BERGISCHE
UNIVERSITÄT
WUPPERTAL

Bergische Universität Wuppertal
Fakultät für
Mathematik und Naturwissenschaften
Fachgruppe Physik

Angular precision of the roving laser calibration system for the Fluorescence Telescopes of the Pierre Auger Observatory

Bachelor Thesis

zur Erlangung des akademischen Grades Bachelor of Science (B.Sc.) im Studiengang Physik

vorgelegt von Patrick Kleu

Matrikelnr. 1821878

Sommersemester 2021

Erstprüfer:	Prof. Dr. Karl-Heinz Kampert
Zweitprüfer:	Prof. Dr. Ralf Koppmann
Abgabedatum:	20.09.21

Abstract

In this thesis, the angular precision of a telescope mount used for a *roving laser system* is determined. Two different methods for inclination measurements are presented and compared. Furthermore, an approach to determine the azimuth alignment of the mount is taken.

The first method is the inclination measurement using a laser level in the laboratory, which leads to the conclusion that the method is not precise enough to measure the inclination when the mount is set up using the built-in bubble level, as the uncertainty on the inclination is $0.047\,^\circ$ on the measured angle.

The second method uses acceleration sensors measuring the oscillation of the acceleration when the rotation axis is not aligned with the axis of earth's gravitational acceleration. With this method, the accuracy of the mount set up with the bubble level in the basement of the university building can be determined to be $\theta_{\text{Centered}} = (0.067 \pm 0.003)\,^\circ$. Furthermore, the azimuth angle is determined using the acceleration data, which yields an azimuth angle with an uncertainty of $7.84\,^\circ$ in the basement. At last, the same measurements were executed outside of the building to validate the methods with conditions similar to the expected set up place of the mount. The inclination of the mount was determined to be $\theta_{\text{Outside},1} = (0.121 \pm 0.016)\,^\circ$ in a first measurement and $\theta_{\text{Outside},2} = (0.090 \pm 0.005)\,^\circ$ in a second measurement at another location, whereas only the second measurement is significant, since the first measurement is subject to an unknown error. These values are larger than the inclination in the basement but still are in the range of desired accuracy of $< 1\,^\circ$. The azimuth angle of inclination outside of the basement yields an uncertainty of $14\,^\circ$ on the azimuth angle, which is not precise enough to use this information for reducing the inclination more. Both measurements outside of the building can not be used for a precise determination of inclination and azimuth angle at the same time. A further elaboration on the measurement procedure outside of the building is necessary. Nevertheless, with the setup of G-sensor and the software for an automated inclination measurement, a key tool for a successful roving laser campaign has been developed.

Zusammenfassung

In dieser Thesis wird die Winkelgenauigkeit einer Teleskopmontierung für ein *roving laser System* bestimmt, wobei zwei verschiedene Methoden zur Neigungsmessung vorgestellt und verglichen werden. Die erste Methode ist die Neigungsmessung mit einer Laserwasserwaage im Labor, die zu dem Schluss führt, dass die Methode nicht genau genug ist, um die Neigung zu messen, wenn die Montierung mit der eingebauten Wasserwaage aufgestellt wird, da die Unsicherheit der Neigung $0.047\,^\circ$ beträgt. Die zweite Methode verwendet Beschleunigungssensoren, die die Oszillation der Beschleunigung messen, wenn die Drehachse nicht an der Achse der Erdbeschleunigung ausgerichtet ist. Mit dieser Methode kann die Genauigkeit der mit der Wasserwaage im Keller des Universitätsgebäudes aufgestellten Montierung auf $\theta_{\mathrm{Centered}} = (0.067 \pm 0.003)\,^\circ$ bestimmt werden. Außerdem wird der Azimutwinkel anhand der Beschleunigungsdaten bestimmt, was zu einem Azimutwinkel mit einer Unsicherheit von $7.84\,^\circ$ im Keller führt. Schließlich wurden dieselben Messungen außerhalb des Gebäudes durchgeführt, um die Methoden unter ähnlichen Bedingungen wie am erwarteten Aufstellungsort der Montierung zu validieren. Die Neigung der Montierung wurde bei einer ersten Messung zu $\theta_{\mathrm{Outside,1}} = (0.121 \pm 0.016)\,^\circ$ und bei einer zweiten Messung an einem anderen Ort zu $\theta_{\mathrm{Outside,2}} = (0.090 \pm 0.005)\,^\circ$ bestimmt, wobei nur die zweite Messung von signifikanter Bedeutung ist, da die erste Messung fehlerbehaftet ist. Diese Werte sind größer als die Neigung im Keller, liegen aber noch im Bereich der gewünschten Genauigkeit von $< 1\,^\circ$. Der Azimutwinkel der Neigung außerhalb des Kellergeschosses ergibt eine Unsicherheit von $14\,^\circ$, was nicht genau genug ist, um diese Information für eine weitere Verringerung der Neigung zu verwenden. Beide Messungen außerhalb des Gebäudes können nicht für eine genaue Bestimmung von Neigung und Azimutwinkel gleichzeitig verwendet werden. Eine weitere Ausarbeitung des Messverfahrens außerhalb des Gebäudes ist hier nötig. Mit dem Setup des G-Sensors und der Software für eine automatisierte Neigungsmessung wurde jedoch ein wichtiges Instrument für eine erfolgreiche Roving Laser Kampagne entwickelt.

Contents

List of Figures

List of Tables

1 Introduction

Measuring cosmic rays reaching Earth is one of the main methods to understand various events taking place outside of earth's atmosphere, the solar system and even the milky way galaxy. To measure such cosmic rays, large observatories like the *Pierre Auger Observatory* in Argentina are necessary. For such an observatory, it is of high importance to run both relative and absolute calibrations, to ensure the cosmic rays captured by the observatory can be examined with high precision.
The main goal of this thesis is to determine the angular precision of such a calibration setup, the roving laser. With roving laser campaign an absolute calibration of the Fluorescence telescopes at the Pierre Auger Observatory can be performed. The calibration is done using a high energy laser. The laser light scattered in the atmosphere can be measured by the fluorescence telescopes. To work out such a calibration campaign with high precision, it is important to know the inclination of the laser with respect to zenith and the azimuthal direction of inclination. A high inclination has several effects on the measurement, making the calibration more difficult. The determination of this inclination is done using two different methods. The first method makes use of a laser level in the laboratory to determine the inclination of the mount when it is set up as precise as possible using the built in bubble level. The second method uses acceleration sensors, to both determine the angle of inclination as well as the azimuth angle of inclination.

The structure of this thesis is as follows: Chapter 2 gives the necessary theoretical fundamentals for the Pierre Auger Observatory as well as the methods used later in the experimental part. Chapter 3 is the main experimental part, structured in several subsections, beginning with a calculation of the necessary angular accuracy in Chapter 3.1. Chapter 3.2 deals with the inclination measurement using the laser level. Chapter 3.3 focuses on the inclination measurement with the G-sensor setup and the necessary measurements around this setup. In Chapter 3.3.9 an approach to determine the azimuth angle of inclination is given. Chapter 3.4 is about the angular accuracy of the setup when it is placed outside the laboratory on an uneven ground. In the last part, Chapter 4, a brief summary of this work is given.

2 Theoretical foundations

The first chapter gives a brief overview about the context of this thesis. First, cosmic rays and their measurement via air showers are introduced. Thereafter, the Rayleigh-scattering in the atmosphere is briefly outlined. Finally, the methods of measurement used in this thesis are presented.

2.1 Cosmic rays

Viktor Hess first discovered the circumstance that the degree of ionization of the atmosphere is getting higher, the higher the altitude gets at which the ionization is measured [1]. Using a balloon, flying maximum 5.350 kilometers high, he measured the degree of ionization for different heights. Concluding from this measurement he stated that most of the radiation ionizing the atmosphere must come from outer space while losing energy as it passes through the atmosphere [1]. He was awarded with a Nobel prize for his discovery in 1936.
With this new insight an entire new field of research started, the so called particle physics. Given this awareness of radiation coming from outside the earth, numerous new experiments were planned to understand this radiation more.
In 1954 a model describing the interaction of high energy particles, creating particle showers in the atmosphere, was proposed. This model, called *Heitler Model*, describes the propagation of high energy particles in the atmosphere in two parts, the electromagnetic and the hadronic shower. The electromagnetic showers originate from single high energetic photons, interacting with the atmosphere producing electron-positron pairs. As those lose energy via bremsstrahlung, an iteration of pair production is created. Hadronic showers originate from high energetic atomic nuclei, such as a single proton or bigger nuclei like those of helium. These particles generate hadronic cascades, which may include pions and kaons. The neutral pions decay into photons, causing electromagnetic showers. The charged pions interact with nuclei in the atmosphere or decay into muons, protons, neutrons and neutrinos [2]. Figure 2.1 gives a schematic representation of theses showers.

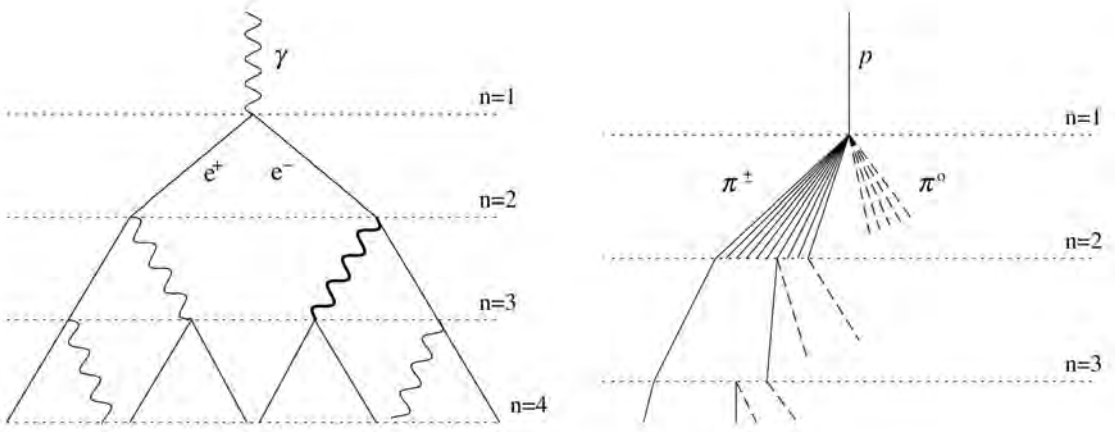

Figure 2.1: Schematic representation of electromagnetic and hadronic air showers. [2]

Particles with low energies have a higher flux than those with high energies, as seen in the energy spectrum in Fig. 2.2.

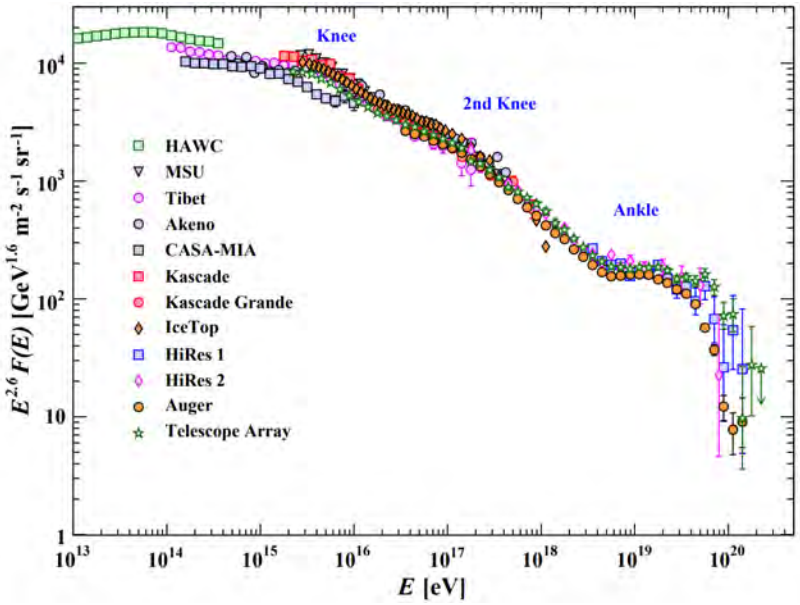

Figure 2.2: The scaled flux of the measured particles as function of the energy E. [3]

This leads to the two possibilities of detection: direct measurement using satellites in the upper atmosphere, measuring the low-energy particles and indirect measurement of the high energy particles at lower altitudes. The high energy particles need a big detection volume, as the flux is considerably lower than the flux of low energy particles. For these measurements, it is common to use the Earth's atmosphere as a calorimeter and detect these particles using big arrays of detectors.

2.2 The Pierre Auger Observatory

The largest observatory detecting cosmic rays is the *Pierre Auger Observatory* in Argentina near Malargüe in the province Mendoza. The observatory covers an area of about $3000\,\mathrm{km}^2$ with 1660 Water-Cherenkov-detectors, 24 air-fluorescence telescopes and three high elevation fluorescence telescopes [7]. In the following the fluorescence telescopes are described in detail, as these are the main subject of this thesis.

2.2.1 Fluorescence detectors

Key properties of cosmic ray showers can be determined by the detection of photons emitted by nitrogen fluorescence induced by cosmic ray particles. As the charged particles of extensive air showers excite nitrogen molecules in the atmosphere, the excited molecules emit fluorescence light with a wavelength of $300-430$ nanometers. Measuring the amount of fluorescence emission in relation to the atmospheric depth X, one receives the longitudinal development profile $\frac{dE}{dX}(X)$ of the air shower.This gives roughly $90\,\%$ of the total dissipated energy of the primary cosmic ray through integration [9]. The atmospheric depth is given by

$$X(h,\theta) = \frac{1}{\cos\theta} \cdot \int_h^\infty \rho(h)\, dh \tag{2.1}$$

with the height, h, the inclination angle of the incoming particle in respect to zenith, θ and the atmospheric density, ρ [8]. Multiple types of scattering change the distribution the total light yield detected by fluorescence detectors in addition to the measured fluorescence light (see chapter 2.3).

The detection of such fluorescence light is realized at the Pierre Auger Observatory using the fluorescence detector (FD) consisting of four observation sites with six independent fluorescence telescopes each. Given a field of view of $30\,^\circ \times 30\,^\circ$, the combination of six telescopes results in a field of view of $180\,^\circ$ in azimuth and $30\,^\circ$ in altitude for one so called 'eye' [9]. The setup of one of telescope is shown in Fig. 2.3a.

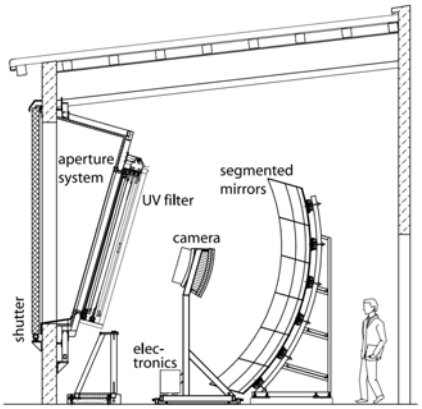

(a) View of one telescope

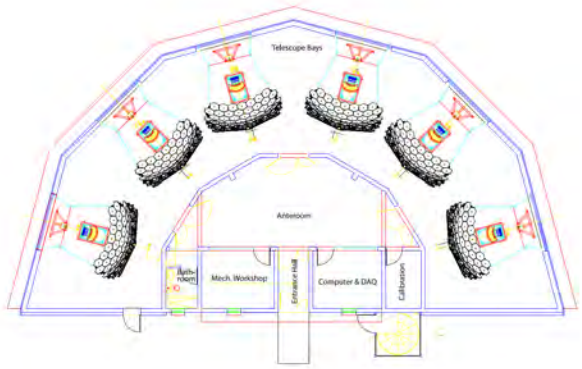

(b) View of the whole detector array

Figure 2.3: Schematic representation of one fluorescence telescope and one whole eye. [9]

Combining six telescopes yields one whole 'eye', as seen in Fig. 2.3b.
The camera used at each fluorescence telescope is made up of 440 pixels positioned in a 22×20 matrix, as shown in Fig. 2.4.

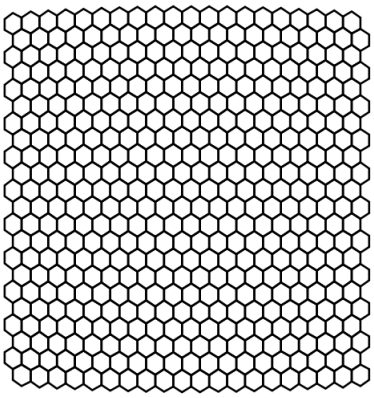

Figure 2.4: The arrangement of the 440 pixels in a 22×20 matrix array for the FDs cameras. [9]

As an air shower is detected, the trace of the air shower is made visible with the FD, as seen in Fig. 2.5.

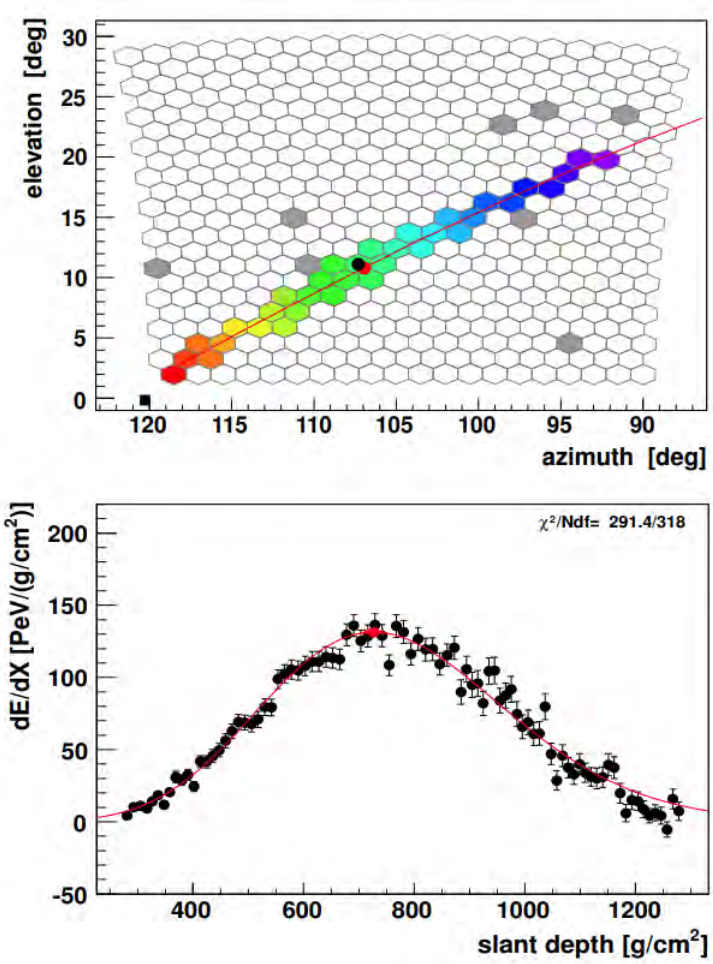

Figure 2.5: An example of an air shower measured with one of the cameras. The upper image shows an air shower as seen by the cameras. The color displays the temporal progress of the air shower, while the x- and y-axes are the azimuth angle and the elevation angle at which the air shower is detected. The lower image shows the differential energy loss measured plotted versus the slant depth or atmospheric depth. The position of the maximum yields information about the type of particle detected with the FD.[7]

2.2.2 Calibration of the telescopes

Reconstructing the air showers with the FD requires calibration of each pixel used in the camera. Relative calibrations can be done with regular measurements. Absolute calibrations are used as a reference for the relative calibrations. They are performed using a calibrated light source and require a lot more work than relative calibration, which is why they are not done on a regular base. With the absolute calibration, the response of each pixel to a set flux of photons can be determined. Also side effects produced by aperture projections and mirror reflections can be measured and taken into account when

measuring real air showers [9]. There have been several other absolute calibration campaigns in 2002, 2003, 2005 and 2006 with different approaches. One approach in 2002 was using a drum-shaped light source, attached from the outside to the FD apertures. The light source provides light pulses of set energy and uniformity throughout the whole light source, which leads to the light drum triggering all pixels of one telescope simultaneously [10].

Another approach is the use of a laser system in the field in front of the telescopes. Using a vertical laser, one can simulate the response of the camera to an air shower with a given energy. The energy of the simulated air shower is determined by the energy of the laser used. As the laser is shot vertically into the sky, the the laser light is measured by each pixel of the detector. The difference to air showers is the temporal progress being inverted, as the laser is going upwards and real air showers are going downwards. With this exact light source, each vertical line of pixels of the fluorescence telescopes can be calibrated. A simulation of such a laser calibration can be seen in Fig. 2.6.

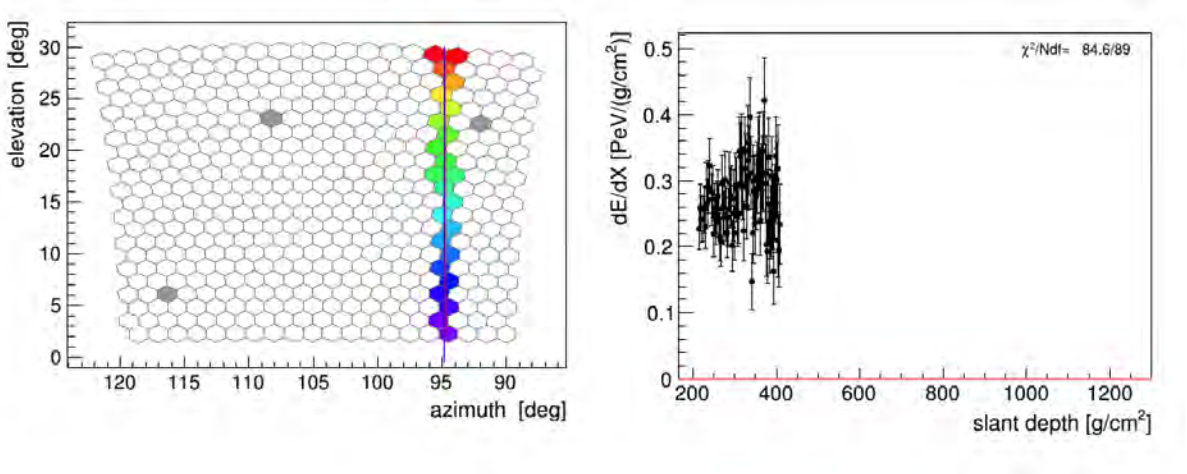

Figure 2.6: A simulation of a vertical laser shot in front of the Coihueco eye in a distance of 4 km. The simulated laser corresponds to a cosmic ray energy of $(2.65 \pm 0.05) \cdot 10^{14}$ eV. The left image shows the laser as detected by the FD. The color of the activated pixels shows the temporal progress of the laser. The image on the right shows the differential energy flux plotted versus the slant depth.[28]

A comparison with Fig. 2.5 shows that the laser is going from the bottom to the top of the camera, whereas a real shower is descending. It can be seen that the plot shows no clear maximum, as the laser shot does not have a maximum of energy dissipation.
There have been several laser calibrations in 2003 and 2005 using nitrogen lasers [11, 12]. As the fluorescence light is emitted towards the detectors, it is scattered by the molecules in the atmosphere between laser and detector, mostly through Rayleigh scattering. The Rayleigh scattering cross section of the atmosphere is known well enough to predict the

flux of photons arriving at the detector.
It is important to know the inclination of the laser precisely, as a high, unknown inclination makes the calibration more complex. The main goal of this thesis is to measure the angular precision of such a setup, used for a new generation of laser calibration system.

2.3 Rayleigh-scattering in the atmosphere

While measuring cosmic air showers by using the atmosphere as a calorimeter, it is important to take Rayleigh-scattering into account, as photons, passing through the atmosphere interact with the molecules the atmosphere is made of. The same occurrence is to be considered when using a laser imitating an air shower for calibration purpose. Most of the interaction can be classified as Rayleigh-scattering, where the photon is scattered on particles, which are small in relation to the wavelength λ of the photon. This scattering process can be described by the total cross section of Rayleigh scattering [4]:

$$\sigma(\lambda) = \frac{24\pi^3 \cdot (n_\mathrm{s}^2 - 1)^2}{\lambda^4 N_\mathrm{s}^2 \cdot (n_\mathrm{s}^2 + 2)^2} \cdot \left(\frac{6 + 3\rho_\mathrm{n}}{6 - 7\rho_\mathrm{n}}\right) \tag{2.2}$$

In this equation λ is the wavelength of the electromagnetic wave, n_s the refractive index for *standard air* at the wavelength λ, $N_s = 2.54743 \cdot 10^{19}\,\mathrm{cm}^{-3}$ the molecular number density for standard air and ρ_n the depolarization factor [4]. Standard air is defined as dry air containing 0.03 % CO_2 by volume at normal pressure 760 mm Hg (= 1013.25 mb) and having an air temperature of 15 °C. [5]. The depolarization factor is a term that takes the anisotropy of an air molecule into account and is dependent of the wavelength [4]. The whole term $F_k = \left(\frac{6+3\rho_\mathrm{n}}{6-7\rho_\mathrm{n}}\right)$ is called the *King-correction factor*. To calculate the angular distribution of unpolarized light scattered by air, the Rayleigh phase function is used:

$$P_\mathrm{ray}(\vartheta) = \frac{3}{4 \cdot (1 + 2\gamma)[(1 + 3\gamma) + (1 - \gamma)\cos^2(\vartheta)]} \tag{2.3}$$

with $\gamma = \frac{\rho_\mathrm{n}}{2-\rho_\mathrm{n}}$ [6]. To calculate the angular distribution for polarized light, the phase function gets more complicated. It is important to take Rayleigh scattering into account, as the different wavelengths of the fluorescence light are scattered in different angles, which would lead to false assumptions about the energy of the photon measured.

2.4 Mount of the laser setup

As seen in Chap. 2.2.2, the telescopes of the FD can be calibrated using a Laser in front of them. To set up such a laser, a stable mount which can also be aimed in several directions is necessary. In this new approach a telescope mount is used. A telescope mount which is suited well for this setup is the Altazimuth Mount *iOptron ® AZ Mount Pro™* [16] with

motor-controlled GOTO-capability, being able to move to a set position automatically, controlled by a hand controller connected to the mount by a cable. The mount can also be controlled by a software or direct commands over a communication protocol. The last method is used later on to automate the mounts movement. The mount can be seen in Fig. 2.7.

Figure 2.7: The telescope mount with the used tripod. [17]

The mount can move in 9 different speeds, with the fastest being around $10\,°/s$ and is equipped with a precision bubble level to align the mount in the field [16].

2.5 Acceleration sensors

In the following, the principle of acceleration sensors and the use of acceleration sensors for inclination sensing is outlined.

2.5.1 Measurement principle of acceleration sensors

In the following an MPU-6050 acceleration Sensor [23] is used to examine the angular precision of a telescope mount. In this chapter the functionality of such an acceleration Sensor is briefly discussed.
To measure static or dynamic acceleration, two types of acceleration sensors can be used: capacitive and piezoelectric sensors. Figure 2.8 represents the capacitive method.

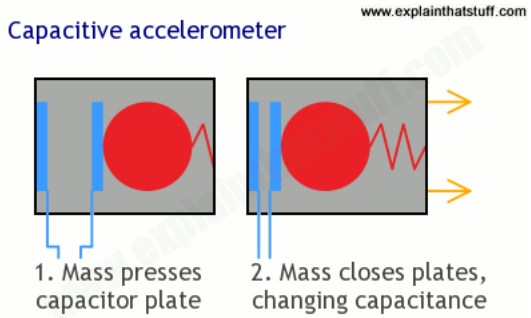

Figure 2.8: The functionality of an acceleration sensor using capacitors for measurement.[18]

Using the capacitive method a mass is fixed inside the sensor at one side and able to move only along one axis (e.g. the x-axis). Additionally, a plate capacitor is placed inside the sensor, with one electrode being fixed on the opposite side of the mass and one electrode being movable. As the sensor is accelerated, the mass will move in the reference frame of the sensor in the opposite direction of the acceleration as it carries an inertial mass. The mass then pushes the movable electrode of the capacitor resulting in a change of the distance between the two electrodes. As the capacity of the capacitor is dependent of the distance of the two electrodes, the capacity changes as the electrode moves. This change in capacity is measurable and can be correlated with the associated acceleration. To measure acceleration in three axes, three of such systems are needed, as one can only measure acceleration along one axis.
The piezoelectric method uses a piezoelectric crystal in place of the capacitor, resulting in a measurable voltage output when the crystal is deformed by the mass.
To realize this setup in a tiny sensor like the MPU-6050, no swinging mass is used. In microelectronics, one electrode is mounted freely movable, as pictured in Fig. 2.9.

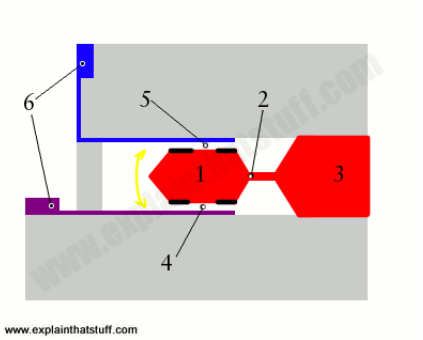

Figure 2.9: The brief functionality of acceleration sensors realized in microelectronics. The movable electrode (red, 1) is now placed in between two fixed electrodes (blue and purple, 4 and 5), forming two capacitors. The link (red, 2) is built in such way that it allows the electrode to move, but is stiff enough to prevent it from breaking. The black pads are insulators, preventing a short circuit when the acceleration is high enough so that the flexible electrode would contact either of the fixed ones. The change in capacity is measured between 3 and 6. [18]

Using this setup, a change in capacity will be measured on acceleration on both capacitors, in spite of the acceleration direction. This setup is called *Micro Electro Mechanical System accelerometer* and is used in most microelectronic setups [18].

2.5.2 Calculating the inclination using acceleration data

Given an acceleration sensor in the gravitational field of the earth, the inclination of the sensor can be calculated. To do so, the sensor needs to consist of three individual sensors for each axis, giving acceleration data in all three axes. An outline of this inclination can be found in Fig. 2.10.

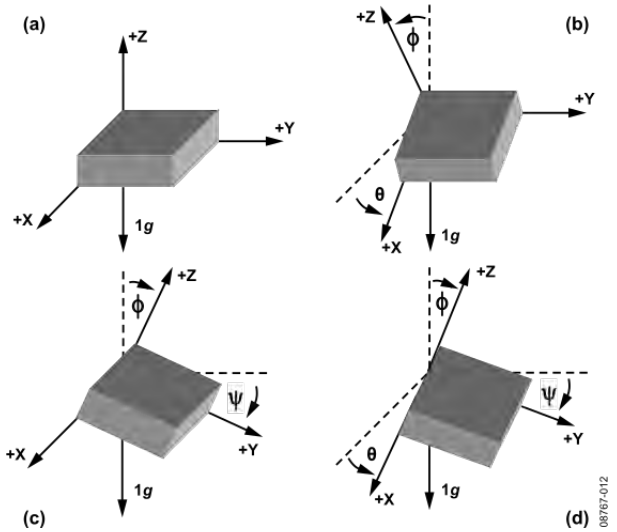

Figure 2.10: An outline of the angles that can be calculated through acceleration data. [19]

The equations to calculate all three inclination angles as seen in Fig. 2.10 are given by equations 2.4 - 2.6 [19]:

$$\theta = \tan^{-1}\left(\frac{A_X}{\sqrt{A_Y^2 + A_Z^2}}\right) \tag{2.4}$$

$$\psi = \tan^{-1}\left(\frac{A_Y}{\sqrt{A_X^2 + A_Z^2}}\right) \tag{2.5}$$

$$\phi = \tan^{-1}\left(\frac{\sqrt{A_X^2 + A_Y^2}}{A_Z}\right) \tag{2.6}$$

The A_i in these equations are the acceleration measured in direction $i \in \{\mathrm{X,Y,Z}\}$. The measured accelerations are relying on a precise calibration of the sensors. Therefore, the equations are not useful if no precise calibration can be done. To bypass this imprecision, a relative measurement of acceleration throughout rotation is used later on.

2.6 Statistical measurements and uncertainties

To calculate the mean value of a statistical measurement, Eq. 2.7 is used.

$$\bar{x} = \frac{\sum_i x_i}{N} \tag{2.7}$$

In this equation, $\bar{x}$ is the mean value, x_i is the value of each measurement i and N the amount of measurements. The standard deviation of the measurements from the mean value is given by Eq. 2.8.

$$\sigma_\mathrm{x} = \sqrt{\frac{1}{N-1}\sum_{\mathrm{i}=1}^{N}(x_\mathrm{i} - \mu)^2} \tag{2.8}$$

The uncertainty of a measurement is defined by the standard error on the mean value, given by Eq. 2.9 [27].

$$\sigma_\mu = \frac{1}{\sqrt{N}} \cdot \sigma_\mathrm{x} \tag{2.9}$$

3 Measuring the inclination of a telescope mount

This chapter deals with the inclination measurement of the telescope mount described in Chap. 2.4. At first, the necessary angular accuracy will be calculated. After that the inclination is determined using both a laser level and acceleration sensors. At last, an approach for determining the azimuth angle of inclination is given.

3.1 Calculating the necessary angular accuracy

To verify the laser being as vertical as needed, it is important to calculate how much deviation from the exact vertical alignment is justifiable. This can be done by taking a look at the angle α between the azimuthal line of sight of two adjacent pixels in the top rows of the telescopes. With this angle α and the altitude angle of each pixel, one can calculate the height of the point the pixel is pointing at in a given distance. In this case the distance is determined by the setup of the laser. The distance will be estimated with 4000 m. With trigonometric calculations the maximum inclination of the laser mount can be determined. With an deviation lower than the calculated one, the laser will activate a maximum of three columns of pixels. To calculate this angle, the minimum angular distance of all pixels is calculated to be $\alpha_{\text{min}} = 1.68\,^\circ$ [13]. The distance between the points, at which two adjacent pixels with a minimum angular distance point in 4000 m distance to the telescopes is 135 m. Using this distance and an approximate setup of the laser in 4000 m distance of the FD yields a maximum angular deviation of the vertical of $\varphi = 1.69\,^\circ$ using trigonometry. Figure 3.1 demonstrates this maximum angle.

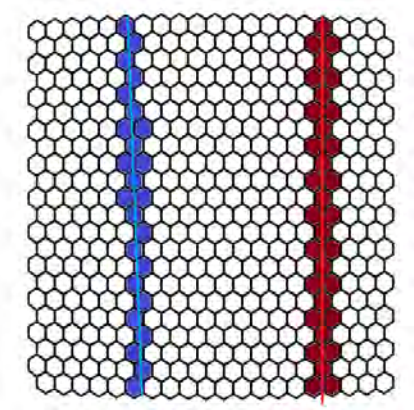

Figure 3.1: Schematic representation of the maximum inclination of a laser in front of the FD's to activate only one/two rows of pixels.

In this figure, the red line represents a laser going exactly vertical and the blue line an inclined laser. The maximum inclination calculated is the inclination, at which the laser does not activate more than three columns of pixels. By simulating a laser calibration, it

can be seen that an activation of adjacent pixels can already be seen at an angular offset of 1° [14]. With this information, it is preferable to get an angular precision of $< 1\,°$.

3.2 Inclination measurement with a laser level

To measure the inclination of the telescope mount, a *BOSCH* Laser-Level [20] is used. This device lights a horizontal and a vertical line on a wall using a laser. The laser level can be operated in two modes: static and self-levelling. The self-levelling mode is used to align the vertical line parallel to zenith and the horizontal line in a right angle to the vertical, giving a reference point of what is 'level'. The laser level can be tilted up to 4° in self-levelling mode.
To measure the inclination of the telescope mount, the laser level is attached on the mount. The setup of the laser level on the mount can be seen in Fig. 3.2.

Figure 3.2: The picture shows the laser level attached to the telescope mount.

First, a reference is marked with the laser level in self-levelling mode. This reference line is the shortest distance from laser level to the wall. To eliminate an offset of the laser caused by the attachment on the mount, the laser level is set to static mode. Now the laser level will be moved until the line is coherent with the previously marked reference. To determine the inclination, the mount is then turned one full rotation, where every $30\,°$ of the whole rotation, the mount is stopped and another line in self-levelling mode is marked on the wall. This fraction is arbitrary, a smaller fraction could result in a higher precision but is not achievable in the laboratory, as not all walls are accessible. Then the laser level is again set to static mode and the difference d between levelled and unlevelled beam can be measured for every previously marked position. The biggest distance is then taken for the further calculation. Figure 3.3 shows the geometric setup.

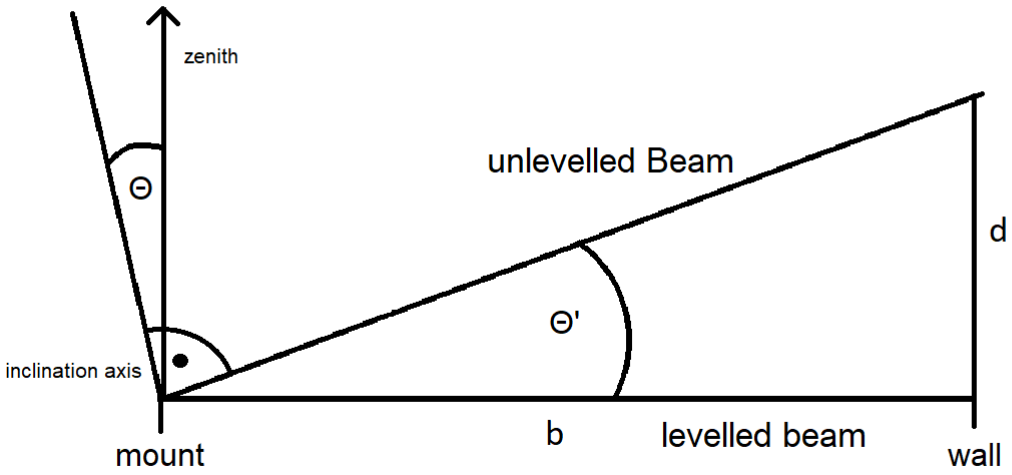

Figure 3.3: Schematic representation of the laser level method to determine the inclination. d is the distance between levelled and fixed beam on the wall and b the distance from laser level to the wall, the angles θ' and θ are equal.

Using this, the inclination with respect to zenith of the mount can be calculated by the following formula:

$$\theta = \arctan\left(\frac{d}{b}\right) = \theta'. \tag{3.1}$$

3.2.1 Accuracy of the laser level

To use the laser level for an accurate measurement of inclination, it is necessary to determine the accuracy of the laser level in self-levelling mode. The resulting uncertainty is directly correlated to the accuracy of the inclination measurement. To measure the accuracy, the laser beams on top and on the bottom side of the laser level are used. Both laser beams are expected to align with zenith when the laser level is set to self-levelling mode. By measuring the deviation from the zenith alignment of these beams, the uncertainty of levelling can be directly derived. The laser level is placed on a mount allowing it to be freely turned, while the bottom laser beam is not moving. At first, the position of the bottom beam is marked on the ground. It is important to ensure the bottom beam is staying on the mark on the ground throughout the measurement. Now a mirror is placed above the laser level, directing the upper beam in a 90 ° angle on the wall instead of the ceiling. By this, the distance the beam travels is enlarged and the beam is accessible for the measurement, which is described in the following. The laser level is now turned in 45 ° steps around the zenith axis, with the position of the beam marked on the wall for every step. If the levelling is ideal, the position of the upper beam on the wall should stay

in one position. If this is not the case, the position of the beam will move in a circular path. Measuring the radius of this circular path directly yields the deviation of zenith alignment. To calculate the angular deviation, Eq. 3.1 can be used, with d being the radius r of the circular path.
For the accuracy measurement, the distance from laser level to the wall, including the distance of the laser level to the mirror is measured to be

$$b_{\text{Accuracy}} = (3790 \pm 10)\,\text{mm}.$$

The radius of the circular path of the beam is measured with

$$r = (3.1 \pm 0.5)\,\text{mm}.$$

The accuracy k is the uncertainty of the laser beam on the wall being level over the distance between wall and laser level and is therefore given by

$$k_{\text{exp}} = \pm\frac{3.1}{3.790}\,\frac{\text{mm}}{\text{m}} = \pm 0.8\,\frac{\text{mm}}{\text{m}}.$$

Using these measurements and Eq. 3.1 yields an angular uncertainty of the self-levelling of

$$\Delta\theta_{\text{exp}} = (0.047 \pm 0.007)\,^\circ.$$

The instruction manual of the laser level [20] names the level accuracy to be

$$k_{\text{theo}} = \pm 0.3\,\frac{\text{mm}}{\text{m}}.$$

This accuracy can also be calculated to an angular accuracy using Eq. 3.1. This yields an accuracy of

$$\Delta\theta_{\text{theo}} = (0.0172)\,^\circ.$$

Comparing the measured accuracy and the accuracy given in the instruction manual yields a deviation of about $0.03\,^\circ$. This deviation can be explained by the laser level not being calibrated ideally or the calibration was influenced by an impact. Furthermore it can not be assured, that the bottom beam was in the exact same position throughout the measurement. Also temperature differences can affect the accuracy of the laser level. The theoretical value of accuracy is given for optimal conditions of measurement. For further calculations, the determined accuracy of k_{exp} and respectively $\Delta\theta_{\text{exp}}$ will be used.

3.2.2 Large inclination measurement

In the first part of this measurement series, the inclination of the mount will be determined with the laser level at a large inclination to validate the sequence of measurement. To achieve this large inclination, the mount is inclined using the fine-tuning screws. Only one screw will be turned until the bubble level is at its outer boundary. With the inclined mount, the measurement sequence as described in Chap. 3.2 is performed and the distance d for every step of the rotation is measured. The position of the mount is marked on the ground to ensure the distance of the laser level to the wall is constant for each position of measurement throughout the various measurements. The distance b for every angle can be found in Tab. 3.1.

Table 3.1: Measured distances b between laser level and wall for every azimuth angle φ at a large inclination.

φ [°]	30	60	90	120	150	180
$b \pm 10$ [mm]	2770	3080	3860	3630	4640	2700
φ [°]	210	240	270	300	330	360
$b \pm 10$ [mm]	2520	3220	3590	3390	3390	3710

To prepare the measurement, the mount is turned to every set angle and the bottom end of the levelled laser beam on the wall is marked. By this, the distance d can be measured for every angle without touching the mount or the laser level, which could change the setup to the point of reference, leading to inaccurate measurements. Then the mount is turned again using the hand controller, with the laser level in static mode. Every 30°, the mount is stopped and the vertical line of the laser level is aligned with the previously marked vertical line on the wall. Afterwards, the distance b between marked horizontal line and the horizontal laser line is measured using a ruler with millimeter marks. For a precise measurement, the bottom end of the laser line is used to measure, as the reference line in self levelling mode is also marked using the bottom end of the laser line. Figure 3.4 shows an example measurement done with the laser.

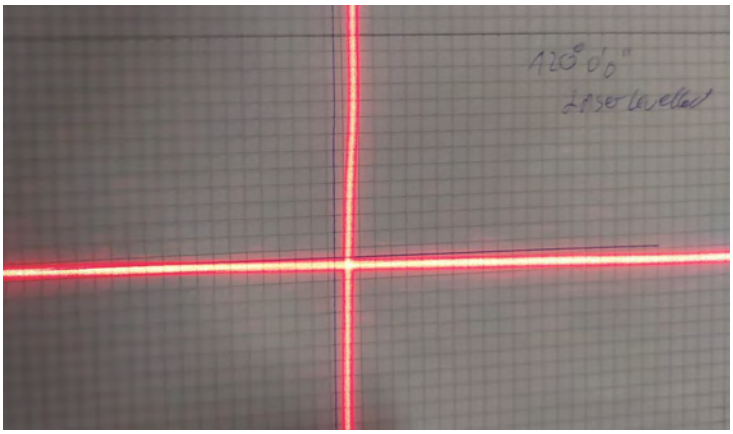

Figure 3.4: The picture shows an example for a measurement done with the laser level. The offset from the previously marked, levelled line can be seen.

The measurement as seen in Fig. 3.4 is done for every angle.
The measured distance d for every angle can be found in Tab. 3.2.

Table 3.2: Measured distances d of the offset between levelled and unlevelled laser for every azimuth angle.

Azimuth angle φ [°]	30	60	90	120	150	180	210	240	270	300	330	360
Distance $d \pm 0.5$ $[mm]$	-13	-12	-8	-7	3	16	11	12	11	6	-2	-5

To calculate the inclination, the highest distance d_{max} is used with the respective distance b. This is because around the smallest value of d, the calibration of laser level and mount is performed. Using Eq. 3.1, this yields an inclination of

$$\theta_{\text{Inclined}} = (0.198 \pm 0.046)\,^\circ$$

The uncertainty on this value is calculated using Gaussian error propagation, as described in Appendix A.1. The reading error on the d value is negligible, as the uncertainty given by the level accuracy of the laser level is significantly higher.

3.2.3 Bubble level accuracy

In this section, the accuracy of the setup using the bubble level is determined using the laser level procedure. The mount is set up in the laboratory in the same way as in Chap. 3.2.2, giving the same values for the distances b as seen in Tab. 3.1. The mount is aligned with zenith using the bubble level on the mount and the three fine-tuning screws. When the bubble level seems to be as centered as possible, all screws on the mount are tightened and the bubble level is checked again. If it has moved, the fine-tuning screws are used to center it again. When the centering is done, the reference points on the wall are

marked and the laser level is again adjusted at one angle like described before. Executing the measurement procedure yields the distances d for every angle as shown in Tab. 3.3.

Table 3.3: The table shows the measured distances d for every azimuth angle with the mount aligned with the bubble level.

Azimuth angle φ [°]	30	60	90	120	150	180	210	240	270	300	330	360
Distance $d \pm 0.5$ $[mm]$	3	3.5	4	4	3	2	1	1	0.5	0	0.5	1.5

Using the largest value for d, the inclination can be calculated using Eq. 3.1:

$$\theta_{\text{Centered}} = (0.059 \pm 0.047)\,^\circ$$

This value cannot be taken for a significant measurement of the precision of the bubble level, as the uncertainty is of the same magnitude as the value itself. Such high uncertainty is the result of both the inaccuracy of the laser level and the reading error on the distance b from laser level to wall. The uncertainties could be minimized by using a more precise tool to measure the distance b, such as a laser-assisted distance measurement tool. Moreover, the laser level could be more precise, as the measured accuracy of the laser level deviates around $0.03\,^\circ$ from the uncertainty given in the instruction manual of the laser level. Additionally, the procedure of measurement can only be done in a laboratory prepared for this kind of measurement, as the walls need to be marked and the distance b needs to remain the same throughout the measurement. This method is not suited to measure the accuracy of the bubble level.

3.3 Inclination measurement with acceleration sensors

In this part, another method to determine the inclination of the mount is presented. This method uses acceleration sensors, which can be used outside of the lab. The acceleration sensor used is a 6-axis motion sensors with a built-in gyroscope and an accelerometer (see Chap. 2.5). The sensor can measure angular velocity as well as linear acceleration in all three axes. Furthermore, the sensor is equipped with a 'DMP', the 'digital motion processor', which combines both angular velocity and linear acceleration to calculate the orientation of the sensor. As the code of the 'DMP' is not transparent, we focus on measuring the alignment using only the linear acceleration data.
With the sensor held in a static position, it is able to measure the gravitational acceleration in every component. When the sensor is not moving, the following equality should hold:

$$|\vec{g}| = \sqrt{a_x^2 + a_y^2 + a_z^2}$$

with a_i the acceleration measurement for each of the three components. It is important to note that the sensor may have internal absolute offsets. An approach to these offsets is given in Chap. 3.3.4.
The direction of zenith is given by the opposite of the gravitational vector $\vec{g}$ [15]. Using this information, one can assume the linear acceleration in all three axes should stay invariant when rotating around the axis of $\vec{g}$, and thus also around the zenith axis. Aligning the sensor on the mount in a 45° angle in every axis, the sensor measures the gravitational acceleration equally in all three components, resulting in the highest possible accuracy. While rotating the mount, all three acceleration components can be measured continuously. If the rotation axis is not exactly aligned to zenith, an oscillation of all three components can be measured, which repeats periodically with every whole rotation of the mount.

3.3.1 The G-Sensor used for inclination measurement

The used acceleration sensor is a *StemmaQT MPU-6050* six-axis acceleration and gyrosensor [21]. To control the sensor, a microcontroller is necessary. For this thesis, an *ESPRESSIF ESP32-Wroom-32E* microcontroller [22] with built in Wifi and Bluetooth connectivity is used. The connection of microcontroller to acceleration sensor is displayed in Fig. 3.5.

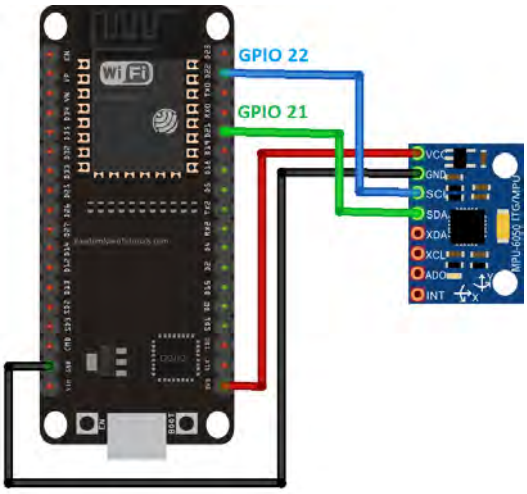

Figure 3.5: Schematic representation of the wiring from the microcontroller to the acceleration sensor. [23]

The wiring is realized using a printed circuit board soldered to both the microcontroller and the sensor. This yields a solid connection between both components, making the setup more stable and easier to tighten in a case, as demonstrated in Chap. 3.3.2. From now on, the setup of microcontroller and acceleration sensor will just be referred to as 'G-sensor'. A program reading out the sensor and writing the values to the serial output has been developed using the *Arduino* [24] software package. These values can be acquired from a PC/Laptop on the USB connection.

The 'G-sensor' is connected to the controlling laptop via micro-USB cable, which also acts as the power supply for the microcontroller. The finished setup of microcontroller, circuit board and acceleration sensor can be seen in Fig. 3.6.

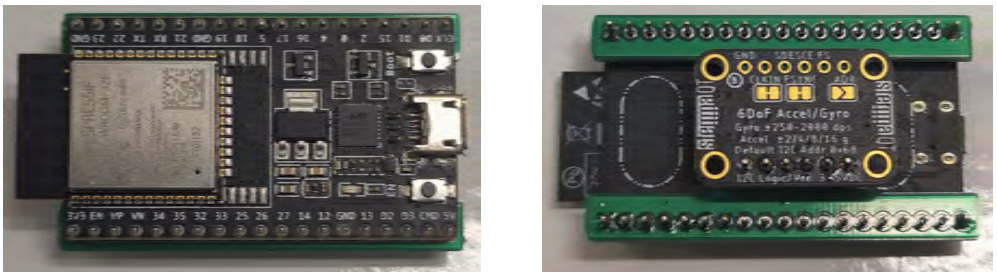

(a) Picture of the ESP-32 microcontroller

(b) The microcontroller connencted to the acceleration sensor

Figure 3.6: The combined G-sensor consisting of microcontroller, circuit board and acceleration sensor.

3.3.2 Attaching the G-sensor to the mount

To attach the G-sensor securely to the mount, a casing is needed which establishes a stable connection of sensor and telescope mount. This can be achieved by 3D-printing a casing, optimized for the dimensions of the sensor and microcontroller setup. The casing is designed using the Freeware *FreeCAD* [25]. Figure 3.7 shows the designed casing with the 45 ° wedge, giving the two of the three needed angles for the attachment of the sensor to the mount. The third angle is achieved by placing the setup in a 45 ° angle on the mount itself.

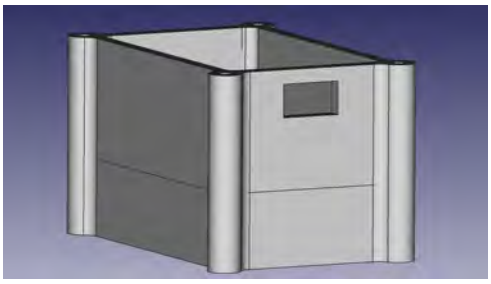

(a) FreeCAD rendering of the Casing, front view

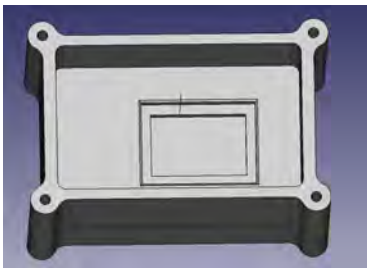

(b) FreeCAD rendering of the Casing, top view

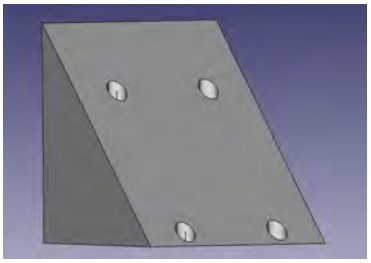

(c) FreeCAD rendering of the wedge

Figure 3.7: FreeCad rendering of the designed case and wedge used to attach the G-sensor to the telescope mount.

The hole on the front of the case is used to plug a power supply to the microcontroller. The top side of the case will be closed using another 3D-printed plate, which is attached to the case using four screws using the boreholes in the cylinders at each corner of the case. To ensure the G-sensor sits tightly in the case, a foam is filled between microcontroller and top plate. By this, the G-sensor does not move inside the case while the case is turned. To improve the stability, the case has an immersion that the G-sensor fits into. Figure 3.7c shows the wedge used to angle the G-sensor in a 45 ° angle on the mount.

The case is attached to a Losmandy dovetail on the mount, which has several holes to tighten screws in it. The whole setup can be seen in Fig. 3.8.

Figure 3.8: Picture of the setup with the G-sensor attached to the mount.

The case is attached using two screws, ensuring that it cannot rotate or move while the mount is turning. For a measurement in the field, the G-sensor with the case will be attached on the rear side of an optical rail, as the dovetail will carry the optical rail carrying the laser components used for the calibration of the FD.

3.3.3 Uncertainty of the G-Sensor

For a precise measurement using the G-Sensor, a measurement is done by taking data over a period of time without moving the sensor. This yields a set of data whose size is dependent of the measurement frequency of the G-Sensor and the time span of measurement. The maximum frequency of the G-sensor is about 31 measurements per second. Over a time span of 15 seconds, this yields about 465 data points. This count is not constant, as the frequency is not constant due to fluctuations in the transmission rate. Figure 3.9 shows such a measurement as an example.

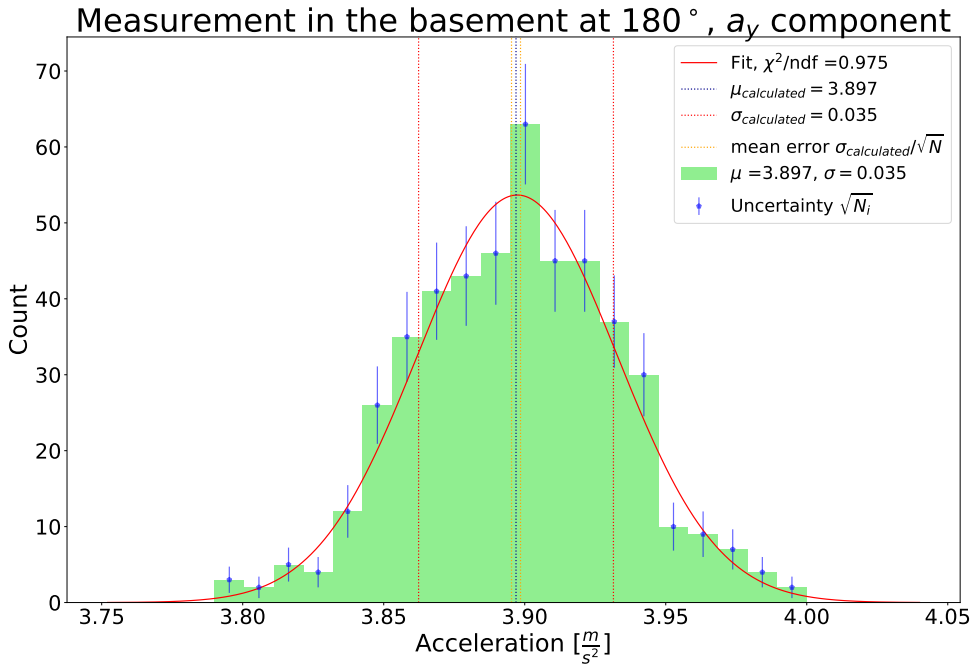

Figure 3.9: A histogram of a measurement of a_y at an angle of 180° done in the basement. The blue dotted line resembles the mean of the data set, the red the standard deviation and the orange the uncertainty of the mean.

With $\chi^2/\text{ndf} = 0.975$, the set of data can be estimated to fit to a Gaussian distribution. The mean value of this set can be calculated using Eq. 2.7 in Chap. 2.6. Additionally, the standard error on the mean is calculated by Eq. 2.9. These calculations yield the data point for a measurement through the mean of the set and the uncertainty of the data point through the standard error.
The fitting parameters for the Gaussian curve in Fig. 3.9 are given in Tab. 3.4.

Table 3.4: The fitting parameters for the Gaussian fit in Fig. 3.9

σ $[\frac{m}{s^2}]$	0.035 ± 0.001
μ $[\frac{m}{s^2}]$	3.897 ± 0.002
A	4.8 ± 0.2
height	53.67 ± 3.13

The fit seems to suit the data set well, as the calculated mean and standard deviation coincide with the mean and standard deviation of the Gaussian fit.

3.3.4 Internal offset of the G-sensor

Using the G-sensor in a static measurement, all three components together should measure roughly earth's gravitational acceleration. Figure 3.10 shows a measurement of all three acceleration components throughout one rotation as described later. The point of interest here is the deviation of $a_{\mathrm{g,exp}} = \sqrt{a_{\mathrm{x}}^2 + a_{\mathrm{y}}^2 + a_{\mathrm{z}}^2}$ from the literature value $g_{\mathrm{theo}} = 9.81099\,\frac{\mathrm{m}}{\mathrm{s}^2}$ [29].

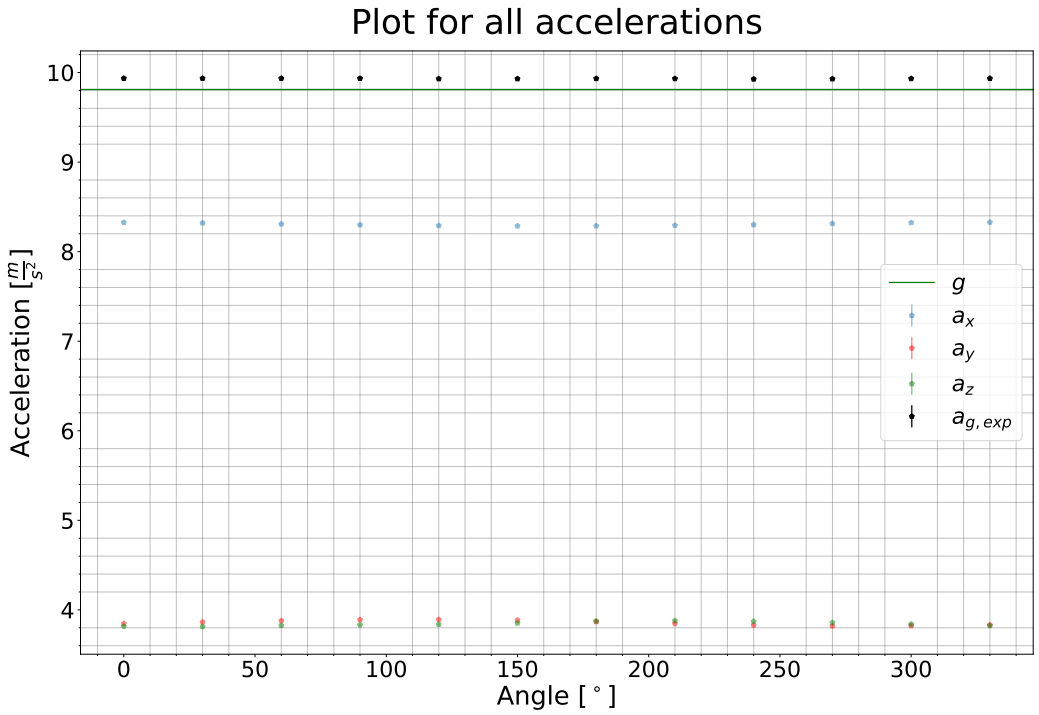

Figure 3.10: The plot shows all three acceleration components as well as the length of the summed vector $a_{\mathrm{g,\ exp}}$ in comparison to the literature value for g_{theo} in Wuppertal [29].

The deviation of a_{x} to a_{y} and a_{z} is due to the G-sensor not exactly angled in a 45 ° angle. This is not of high importance, as the oscillation of each component is more important. To make the offset of $a_{\mathrm{g,\ exp}}$ from g_{theo} more visible, Fig. 3.11 shows only the experimental and theoretical value for g.

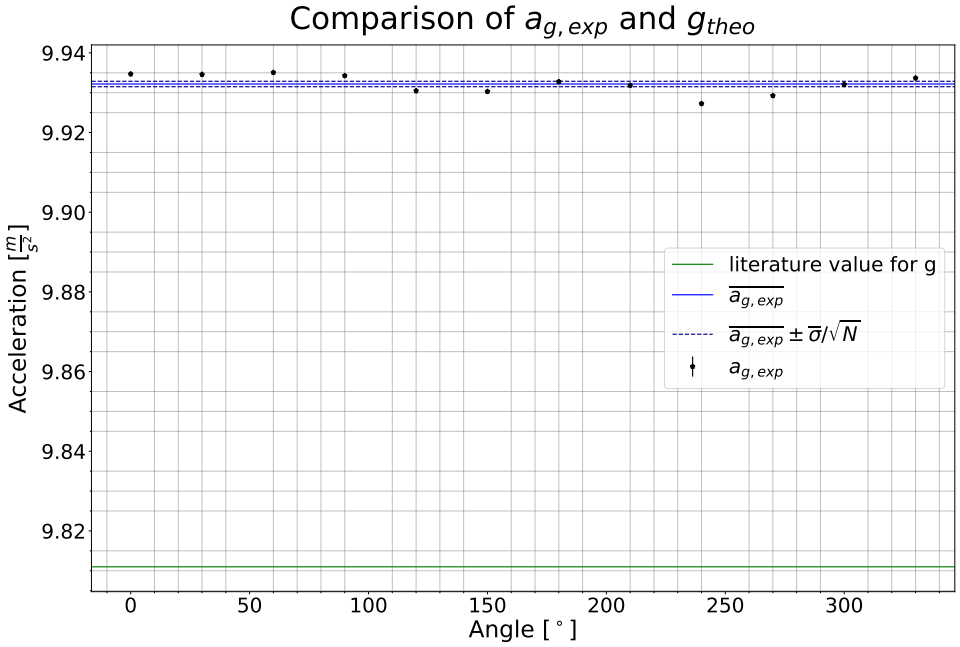

Figure 3.11: The plot shows both g_{exp} and g_{theo} in direct comparison. The offset can be seen clearly.

The blue line in Fig. 3.11 is the mean of the experimental $a_{\text{g, exp}}$ values calculated for each angle and the blue dotted line is the standard error on this mean, calculated with $\bar{\sigma}$ being the standard deviation of the 12 values for g_{exp} of the mean $g_{\text{exp, mean}}$. The green line shows the constant literature value. This offset shows that it is necessary to determine the internal offset of the acceleration sensor used to compute the inclination angle later on. It is sufficient to measure the values of maximum static acceleration for each component. To do so, the sensor is placed on the ground, such that one of the acceleration components gives a maximum value and both other components are minimal. In this position, the sensor is set to take data for a short amount of time. This procedure is done for every component. By that, the acceleration each component is sensing when it should be measuring g_{theo} can be estimated. These measurements are used later, when calculating the inclination. To achieve the acceleration out of every set of data, the mean and the uncertainty on the mean are calculated. The results are shown in the following table.

Table 3.5: The table shows the mean values of the flat acceleration for each component.

	a_x	a_y	a_z
g_i $[\frac{\text{m}}{\text{s}^2}]$	10.4235 ± 0.0008	9.6173 ± 0.0007	9.242 ± 0.001

As this method is not exact, a reference which is level would be needed to determine the offset precisely.

3.3.5 Calculating inclination using the G-sensor data

To determine the inclination of the mount using the G-sensor data, the following calculation is necessary. To make the setup clearer in terms of geometry, Fig. 3.12 shows the telescope mount with the inclination θ to the zenith axis and the geometric dependence of the acceleration measurement.

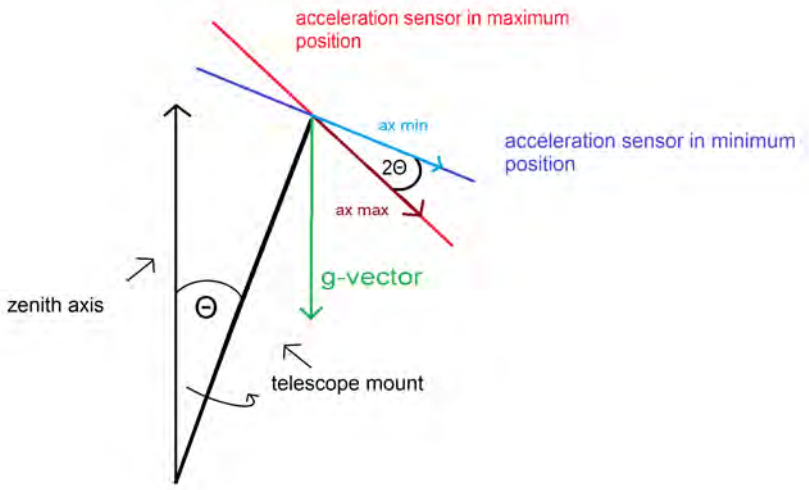

Figure 3.12: Schematic overview of the G-Sensor attached to the telescope mount. By using the angle between maximum and minimum measurement of each component, the inclination angle can be calculated. The blue and red line depict the acceleration measured by one of the components of the sensor in maximum (red) and minimum (blue) position throughout one rotation.

The angle between maximum and minimum yields the inclination of the mount. To determine the angle between both, Fig. 3.13 is helpful.

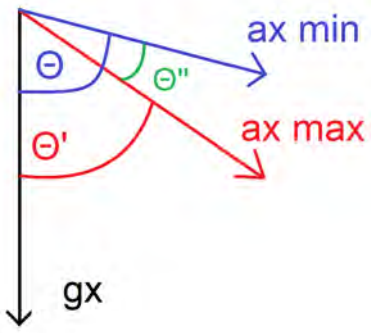

Figure 3.13: Schematic overview of the geometric situation to determine the angle between a_{min} and a_{max}.

Using Fig. 3.13 and Eq. 3.2, each of θ and θ' can be calculated.

$$\cos\theta = \frac{a_{\mathrm{i,\ min/max}}}{g_{\mathrm{i}}} \tag{3.2}$$

In this formula, $a_{\mathrm{i,\ min/max}}$ is the minimum / maximum acceleration each sensor component is measuring and g_{i} the absolute g determined in Chap. 3.3.4 for each sensor component i. To calculate θ'', the difference between θ and θ' is calculated. The inclination of the mount is then given by

$$\theta_{\mathrm{inclination,\ i}} = \frac{\theta''}{2}$$

For a full rotation all three components are measuring the same tilt of the mount. To take all three acceleration components into account, the mean of $\theta_{\mathrm{inclination,\ i}}$ of all three components is calculated, as seen in Eq. 3.3.

$$\theta_{\mathrm{Mount\ inclination}} = \frac{1}{3} \cdot \left(\sum_{i=1}^{3} \theta_{\mathrm{inclination,\ i}} \right) \tag{3.3}$$

3.3.6 Procedure to measure the inclination of the setup

To measure the inclination angle of the telescope mount, the mount is set to make one full rotation around the azimuth axis. While the mount is rotating, the gravitational acceleration in every component is measured by the sensor. To minimize uncertainties, the mount will rotate for an angle of $\varphi = 30\,^\circ$ and then pause the motion. While the mount is not moving, the acceleration will be measured over a time span of 15 seconds. After the measurement, the mount will again slew $30\,^\circ$. This procedure will be done until one whole rotation is finished.

Taking the data for 15 seconds while the mount is stationary minimizes uncertainties, as the mount is vibrating while it is moving. Furthermore, it is not possible to secure that the mount is moving with a constant velocity, leading to acceleration and decceleration throughout the rotation, which would also be measured by the acceleration sensor. For each angle the arithmetic mean and the standard error on the mean of the data taken will be calculated as described in Chap. 2.6. This yields the data point for each angle with the corresponding uncertainty.

To determine the inclination of the mount, the procedure described before will be executed. This is done by a program, controlling the movement of the mount via a communication protocol and direct commands. The same program controls the G-sensor, taking measurements when the mount is not moving. At the end of the measurement procedure, the mount is disconnected automatically. This yields 12 data points for each component of the acceleration. The acceleration data calculated for an example measurement is shown in Tab. 3.6.

Table 3.6: The acceleration data calculated for the example measurement.

Angle [°]	a_x $[\frac{m}{s^2}]$	a_y $[\frac{m}{s^2}]$	a_z $[\frac{m}{s^2}]$
0	8.326 ± 0.001	3.847 ± 0.002	3.818 ± 0.002
30	8.320 ± 0.001	3.864 ± 0.002	3.813 ± 0.002
60	8.308 ± 0.002	3.879 ± 0.001	3.825 ± 0.002
90	8.299 ± 0.002	3.891 ± 0.002	3.831 ± 0.002
120	8.291 ± 0.002	3.892 ± 0.001	3.838 ± 0.002
150	8.287 ± 0.002	3.886 ± 0.001	3.853 ± 0.002
180	8.288 ± 0.002	3.868 ± 0.001	3.876 ± 0.002
210	8.294 ± 0.001	3.847 ± 0.001	3.880 ± 0.002
240	8.300 ± 0.002	3.829 ± 0.002	3.872 ± 0.002
270	8.314 ± 0.001	3.830 ± 0.002	3.858 ± 0.002
300	8.324 ± 0.002	3.822 ± 0.002	3.841 ± 0.002
330	8.329 ± 0.002	3.832 ± 0.001	3.824 ± 0.002

If the rotation axis, and therefore the mount is not aligned with zenith, the data points will oscillate around a given value. One whole rotation of the mount will result in one period of oscillation. The oscillation will perform a sinusoidal curve, which gives further information about the inclination. If the mount is aligned with zenith, the result should be a flat line with no oscillation.

To determine the inclination of the mount using the oscillation of the acceleration data, the amplitude of the sine curves performed by the data points is needed. To attain these values, the data is fitted to a cosine model using python's *LMfit* [26]. The cosine model used is:

$$f(x) = A \cdot \cos(x - B) + C, \tag{3.4}$$

with A being the amplitude of the cosine curve, B the phase and C the offset. As the argument of the cosine, x, is not given an additional factor, the function is forced to perform just one period. Examples of such a measurement with the corresponding cosine fits are given in Fig. 3.14-3.16.

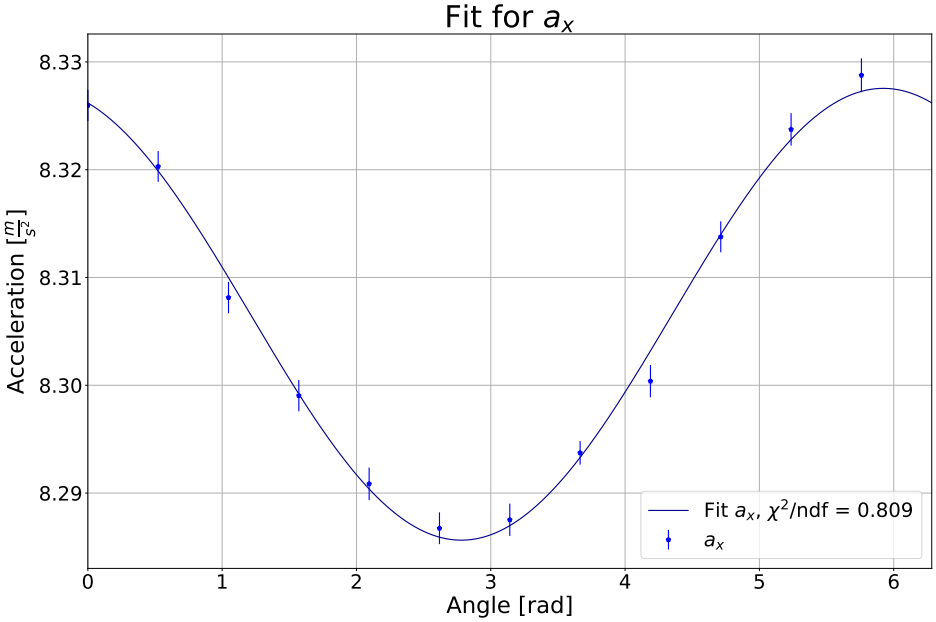

Figure 3.14: The a_{x} component fitted to a cosine curve.

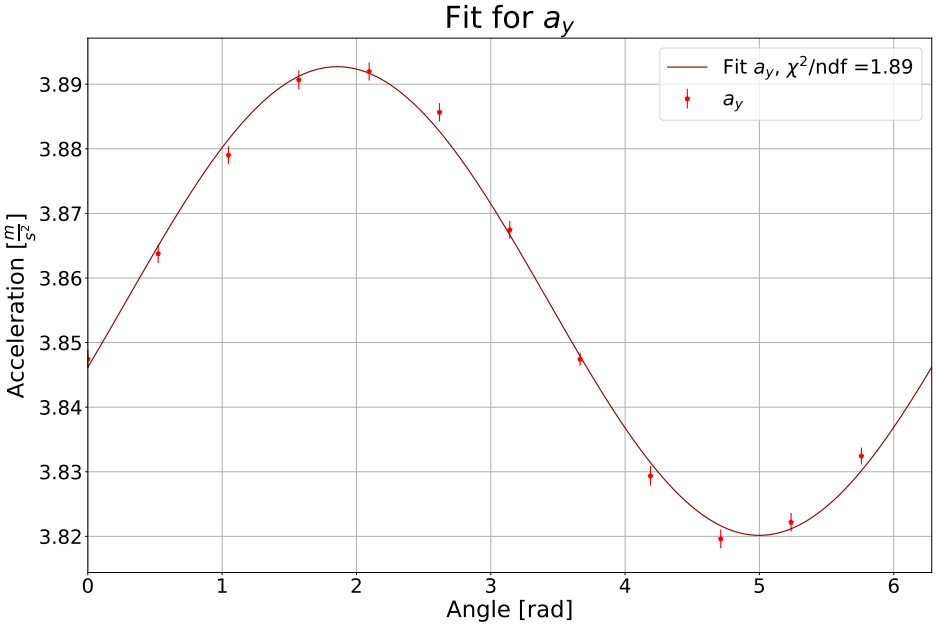

Figure 3.15: The a_{y} component fitted to a cosine curve.

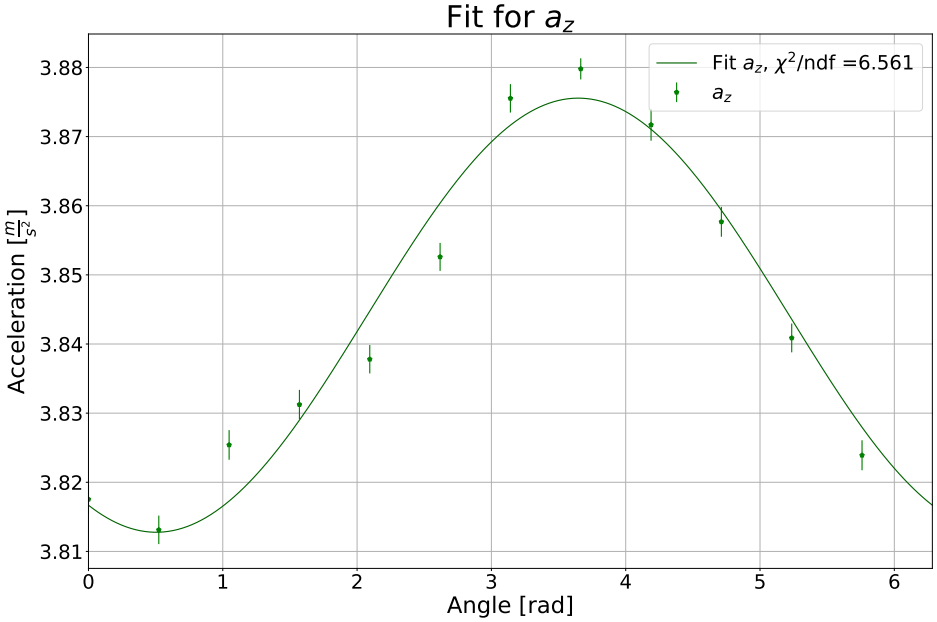

Figure 3.16: The a_z component fitted to a cosine curve.

The angle in each fit is plotted in radiant and later converted to degree. The fit parameters for each fit are given in Tab. 3.7.

Table 3.7: The Fit parameters corresponding to Fig 3.14-3.16.

	a_x	a_y	a_z
Amplitude A [$\frac{m}{s^2}$]	0.0211 ± 0.0005	0.0363 ± 0.0008	0.031 ± 0.002
Phase B [rad]	-0.36 ± 0.02	1.86 ± 0.02	3.65 ± 0.07
Offset C [$\frac{m}{s^2}$]	8.3066 ± 0.0003	3.8564 ± 0.0005	3.844 ± 0.001

Using these fitting parameters and the equations given in Chap. 3.3.5 the inclination of the mount can be calculated. The minimum and maximum acceleration are calculated using the amplitude A and the offset B as given in Tab. 3.7 with the following equation:

$$a_{\mathrm{i,min/max}} = B_{\mathrm{i}} \pm A_{\mathrm{i}}$$

The values for g_{i} are determined in Chap. 3.3.4. This yields an inclination of the mount of

$$\theta_{\mathrm{Example}} = (0.214 \pm 0.004)\,^{\circ}$$

The uncertainty of this value is calculated using Gaussian error propagation, as described in Appendix A.2.

3.3.7 Bubble level accuracy with G-sensor in the basement

In this section, the inclination of the telescope mount when set up in the basement using the bubble level is determined. This yields the angular accuracy of the bubble level.
For this measurement, the bubble in the bubble level is brought to the middle of the circle using the fine-tuning screws of the telescope mount. It is important to ensure that every other screw on the telescope mount is tightened, as every vibrating or moving part can sophisticate the measurement. After tightening every screw, the bubble level is checked again and the mount then is not touched or moved any further.
The turning and measurement controlling is done with a laptop, connected to the mount via Wifi. The whole measurement procedure is performed by an executable python script [30], controlling both mount and G-sensor.
At first, a connection between laptop and mount is established. If the mount is connected successfully, the laptop starts sending commands to the mount, beginning with the mount turning to its *zero position*, which is 180.0 ° azimuth angle and 90.0 ° altitude angle. From now on, the mount will turn in 30 ° steps, while pausing at each position, where the G-sensor measures the acceleration in every component for 15 seconds. After the measurement is done, the mount will turn again. This procedure is repeated until the mount is back at its starting point, where the procedure will be terminated and the mount disconnected. The measured sensor data is saved for each angle of measurement in a different file. For each angle, the mean and the uncertainty on the mean is calculated, as described in Chap. 2.6. The results can be seen in Tab. 3.8.

Table 3.8: The acceleration data calculated for the centered measurement.

Angle [°]	A_x $[\frac{m}{s^2}]$	A_y $[\frac{m}{s^2}]$	A_z $[\frac{m}{s^2}]$
0	8.318 ± 0.002	3.894 ± 0.001	3.808 ± 0.002
30	8.315 ± 0.001	3.897 ± 0.001	3.809 ± 0.002
60	8.314 ± 0.001	3.901 ± 0.001	3.819 ± 0.002
90	8.310 ± 0.002	3.908 ± 0.001	3.816 ± 0.002
120	8.309 ± 0.002	3.907 ± 0.002	3.816 ± 0.002
150	8.306 ± 0.002	3.905 ± 0.002	3.828 ± 0.002
180	8.309 ± 0.002	3.897 ± 0.001	3.832 ± 0.002
210	8.310 ± 0.002	3.893 ± 0.002	3.840 ± 0.002
240	8.310 ± 0.002	3.891 ± 0.001	3.823 ± 0.002
270	8.313 ± 0.002	3.896 ± 0.002	3.820 ± 0.002
300	8.317 ± 0.002	3.889 ± 0.002	3.816 ± 0.002
330	8.318 ± 0.002	3.889 ± 0.002	3.807 ± 0.002

The data is then plotted for each component and fitted to a cosine curve, as described in Chap. 3.3.6. The fits can be found in Fig. 3.17-3.19.

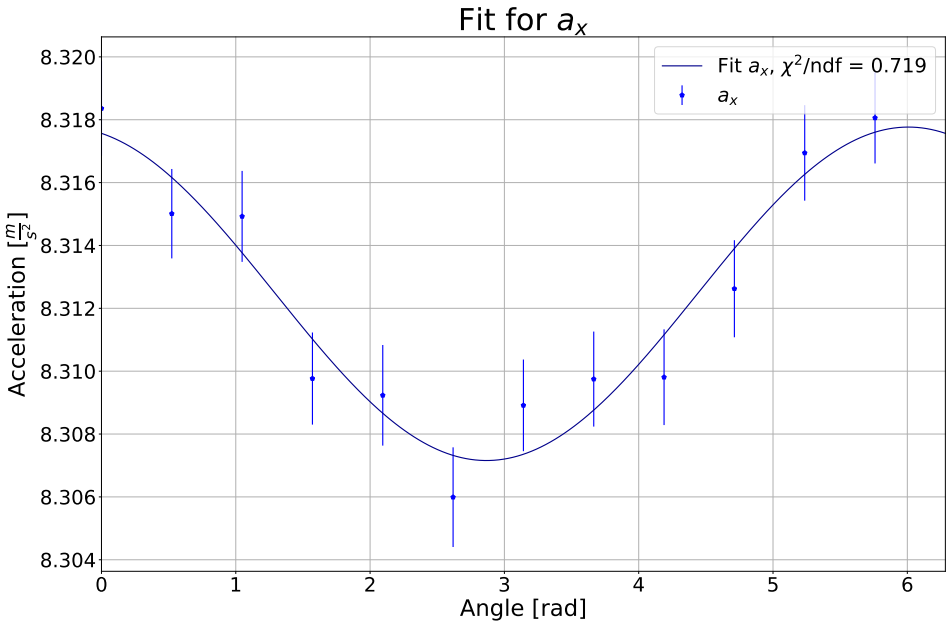

Figure 3.17: a_x component of the centered measurement.

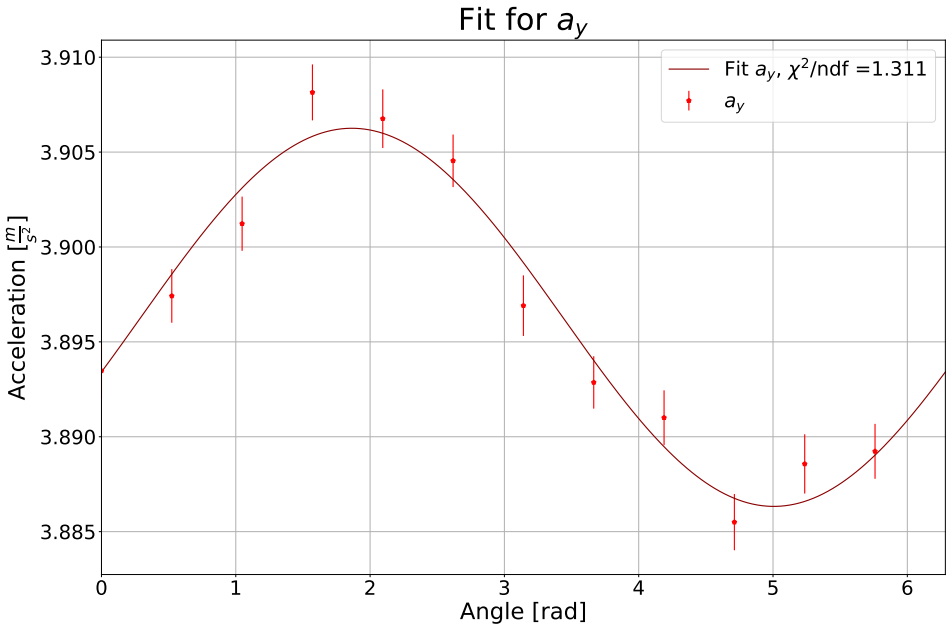

Figure 3.18: a_y component of the centered measurement.

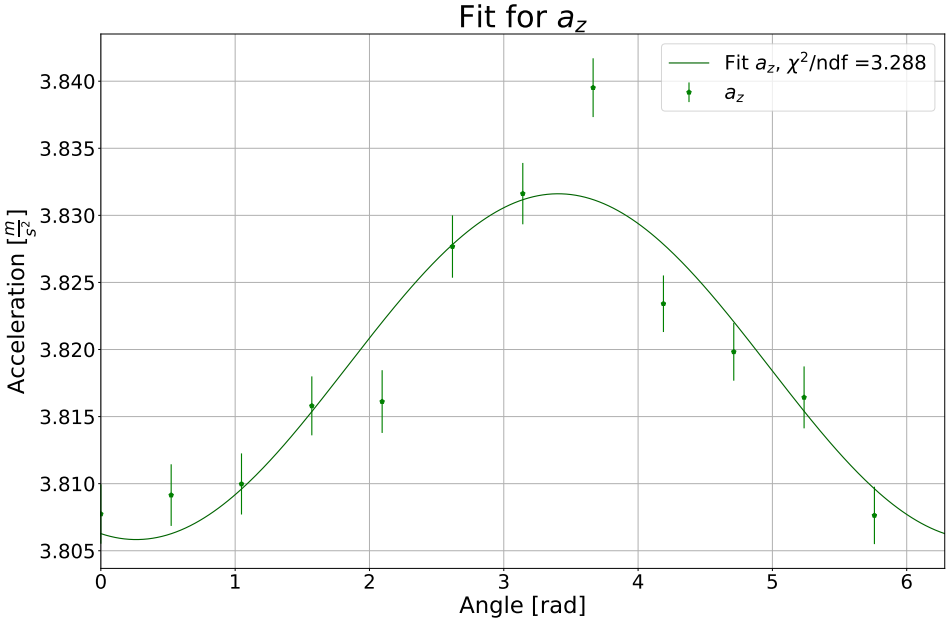

Figure 3.19: a_z component of the centered measurement.

The fitting parameters can be found in Tab. 3.9.

Table 3.9: The Fit parameters for Fig. 3.17-3.19.

	a_x	a_y	a_z
Amplitude A $[\frac{m}{s^2}]$	0.0053 ± 0.0005	0.0099 ± 0.0007	0.013 ± 0.001
Phase B [rad]	-0.28 ± 0.09	1.86 ± 0.06	3.4 ± 0.1
Offset C $[\frac{m}{s^2}]$	8.3124 ± 0.0003	3.8963 ± 0.0005	3.819 ± 0.001

As described in Chap. 3.3.6, the inclination can then be calculated using the amplitude and the offset parameter. The inclination for this measurement is computed to:

$$\theta_{\text{Centered}} = (0.067 \pm 0.003)\,^\circ$$

Comparing this result to the laser level method, one can see that the G-sensor surpasses the accuracy of the laser level method. The uncertainty is 4.5 % for the G-sensor and 79.0 % for the laser level method. To compare the accuracy precisely, the inclination at which the laser level would yield a significant reading has to be determined. The precision of the bubble level can be determined using the angle given by the G-sensor method, as it is the lowest inclination possible using only the bubble level. The difference in precision to the laser level method is founded in several aspects. Firstly, the self levelling mode of the laser level is afflicted with a high inaccuracy. Secondly, measuring

the distances d and b causes uncertainties, as the distances can not be read with high precision. In contrary, the G-sensor method uses no data measured by a human, but all data is taken fully computer operated. Systematic uncertainties can nearly be ruled out, leaving only statistical uncertainties, caused by the sensor measurement being a statistical measurement over a certain time period. Another advantage of the G-sensor method is the possibility to measure the inclination at any arbitrary position, i.e. later in the field. This gives a direct estimation of inclination when the mount is set up in the field with the laser mounted for calibration.
As the G-sensor method allows to determine the inclination in the field, it could also be used to align the mount more precisely than using the bubble level. To do so, it is necessary to know the azimuth angle of inclination, as the mount can not be aligned when the direction of inclination is unknown. The determination of the azimuth angle of inclination is discussed in Chap. 3.3.9. As the accuracy of the bubble level could be determined to be $\theta_{\text{Centered}} = (0.067 \pm 0.003)^\circ$ when used in the basement, a validation of this value outside of the basement is necessary to secure accuracy of the setup placed in the field. The determination of the inclination outside is shown in Chap. 3.4.

3.3.8 Comparing the quality of the G-sensor measurement at different locations

In this section, the quality of the G-sensor measurement at different locations is investigated. The three different locations are

- the basement in the ground floor of the university
- the laboratory in the 5th floor of the university
- a hill outside of the university with no solid ground

Comparing these measurements is important, as vibrations on the floor can impair the measurement of inclination. This is due to the very small amplitude of the cosine curves of the acceleration data, which could be lost in high noise when the ground is vibrating. At first only one static measurement at an arbitrary angle will be examined. To compare the measurements, the data taken by the G-sensor is plotted in a histogram and fitted to a Gaussian curve, to make the deviation of the mean visible. The histograms with the respecting fit can be seen in Fig. 3.20 - 3.22.

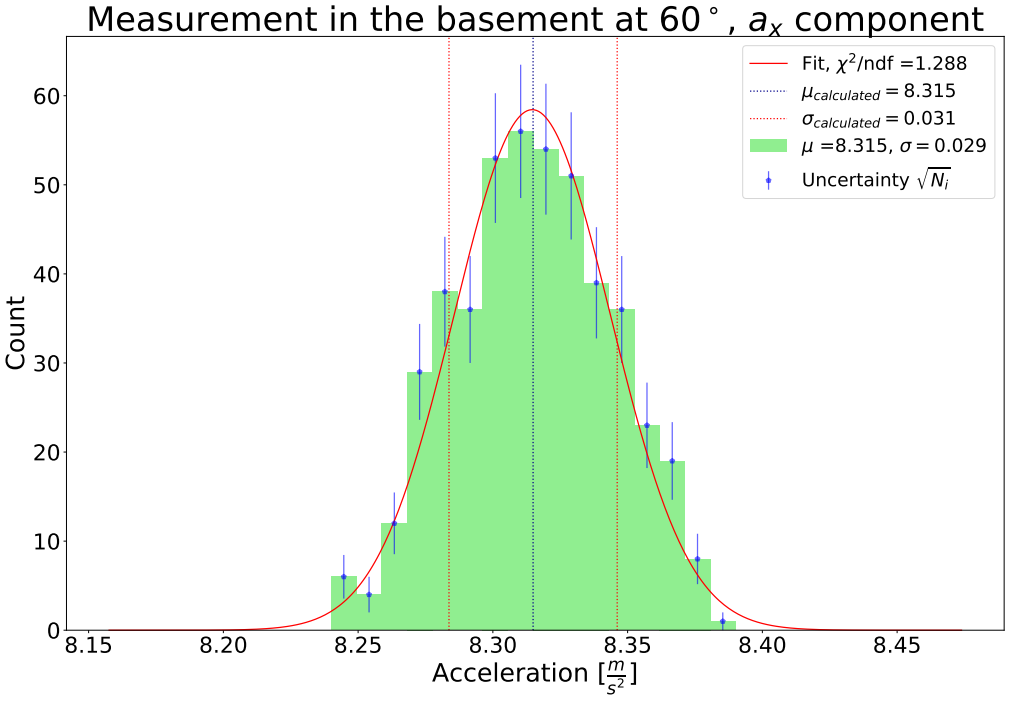

Figure 3.20: The measurement of the a_{x} component in the basement.

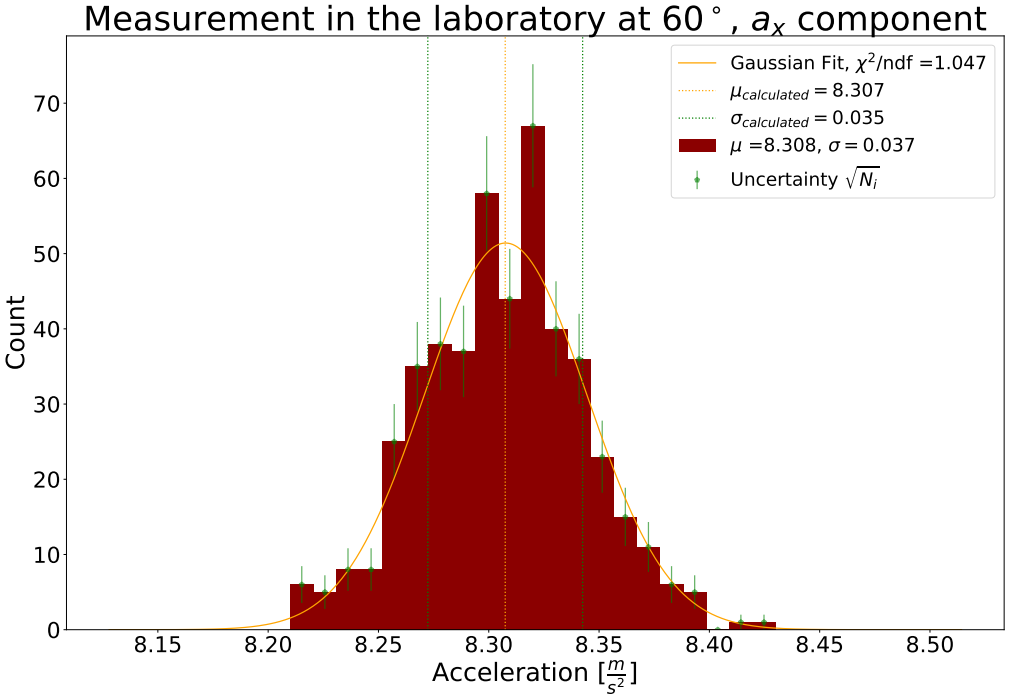

Figure 3.21: The measurement of the a_{x} component in the laboratory.

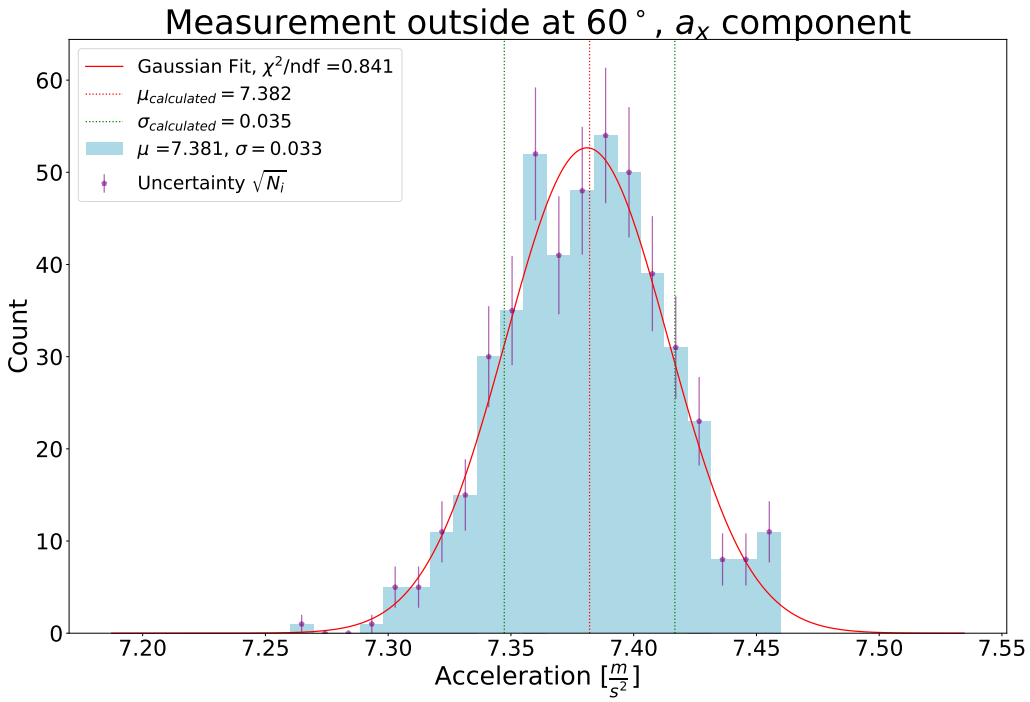

Figure 3.22: The measurement of the a_x component outside.

The Fit is done with a Gaussian model.

The fitting parameters can be found in appendix B. The mean and standard deviation are calculated separately, the results can be found in Tab. 3.10. The standard deviation of the measurement in the basement as well as outside show that the measurements are more precise than the measurement in the laboratory. This could be due to vibrations of the building at an higher elevation. Another reason could be the air conditioning in the laboratory, which could impact the vibration of the ground significantly. To ensure the air conditioning being the source of vibration, another measurement with the air conditioning turned off could be done. Moreover, during the measurement there was construction work in one of the adjacent rooms that could have caused vibrations. As the mount is not expected to be set up in a building later on, it is not that important to localize such vibrations, as they are not having an impact on the measurement for example in the basement. Comparing the standard deviations of the measurements, the measurement in the basement seems to be the most accurate. Comparing the χ^2/ndf of each fit, one can say that each measurement fits well to a Gaussian distribution, which corresponds to the expectation. To compare the different locations accurately, it is important to take all three components into account. Table 3.10 shows the mean and standard deviation values for all three components for different locations.

Table 3.10: The table shows the mean value and the standard deviation for each component at an azimuth angle of 60 ° at the three different locations.

		Basement	Laboratory	Outside
μ $[\frac{m}{s^2}]$	a_x	8.314	8.308	7.382
	a_y	3.901	3.904	5.055
	a_z	3.810	3.862	4.136
σ $[\frac{m}{s^2}]$	a_x	0.031	0.035	0.034
	a_y	0.031	0.033	0.033
	a_z	0.049	0.050	0.057

Table 3.10 shows that the standard deviation for each component is bigger in the measurement outside than in the basement As these values are only for one measurement, it is important to take a look at the standard deviation throughout one whole measurement procedure, to make a significant statement about the difference in precision of the measurement. To do so, the mean of the standard deviations throughout a whole rotational measurement is taken and compared for the different locations. The means can be found in Tab. 3.11.

Table 3.11: The mean value of the standard deviation throughout one whole measurement at different locations.

		Basement	Laboratory	Outside
$\bar{\sigma}$	a_x	0.0327	0.0342	0.0342
	a_y	0.0319	0.0317	0.0322
	a_z	0.0486	0.0497	0.0495

It is noticeable that the standard deviation of the z-component is always bigger than the standard deviation of the both other components. This occurrence is also visible in the fits of the calculations of the inclination angle. The fits for a_z always have the worst χ^2/ndf. A reason for this could be an internal inaccuracy of the acceleration sensor, as all three components should measure with roughly the same precision. Table 3.11 shows the standard deviation in the laboratory is on average 2.05 % bigger than the standard deviation in the basement and the standard deviation outside is 2.4 % bigger than in the basement. The deviation from the basement to the outside could be justified by the machinery close to the location of measurement, such as a wind turbine. Moreover, the measurement was done on a hill, where wind could have an impact on the movement of the mount, too.

3.3.9 Determination of the azimuth angle of inclination

The azimuth angle can be determined using the maxima of the sine fits, as the maxima are the positions of highest acceleration, thus the direction of inclination. These maxima in a system where the sensor is angled in exactly 45 ° should be exactly 120 ° apart. As the sensor is not angled in exactly 45° in each axis, the maxima are not 120 ° apart. Nevertheless, the sum of all distances should stay as 360 °. For each component, the maximum resembles the position of maximum acceleration, thus the inclination axis is in this exact direction. This leads to the conclusion, that the maximum of all three sine curves added together yields the azimuth angle of inclination at the respective maximum of the summed sine curve.
To compute this maximum, the datapoints of all three components are added up. As only the position and amplitude of the maximum is interesting, the offset C will be neglected in the further calculations. As described in Chap. 3.3.4, each component measures the absolute g value differently, which sophisticates simply adding the values without taking the offset of each component into account. This is done by dividing each set of datapoints by the acceleration determined in 3.3.4. These datapoints can then again be fitted to a cosine function:

$$f(x) = A \cdot \cos(x - B)$$

To determine the uncertainty, Gaussian error propagation is used for each datapoint individually. The phase B of the fit yields the position of the maximum. To compare the summed curve with each individual component, the fits for each component are also adjusted to have an offset of zero and divided by their respective g_{i}.

In the following, the azimuth angle of the inclination determined in Chap. 3.3.7 is calculated. Figure 3.23 shows all three fits of Chap. 3.3.7 and the summed curve, adjusted in their Y-offset to zero and normalized by their individual g_{i} as determined in Chap. 3.3.4. The summed curve is determined as described in Chap. 3.3.9.

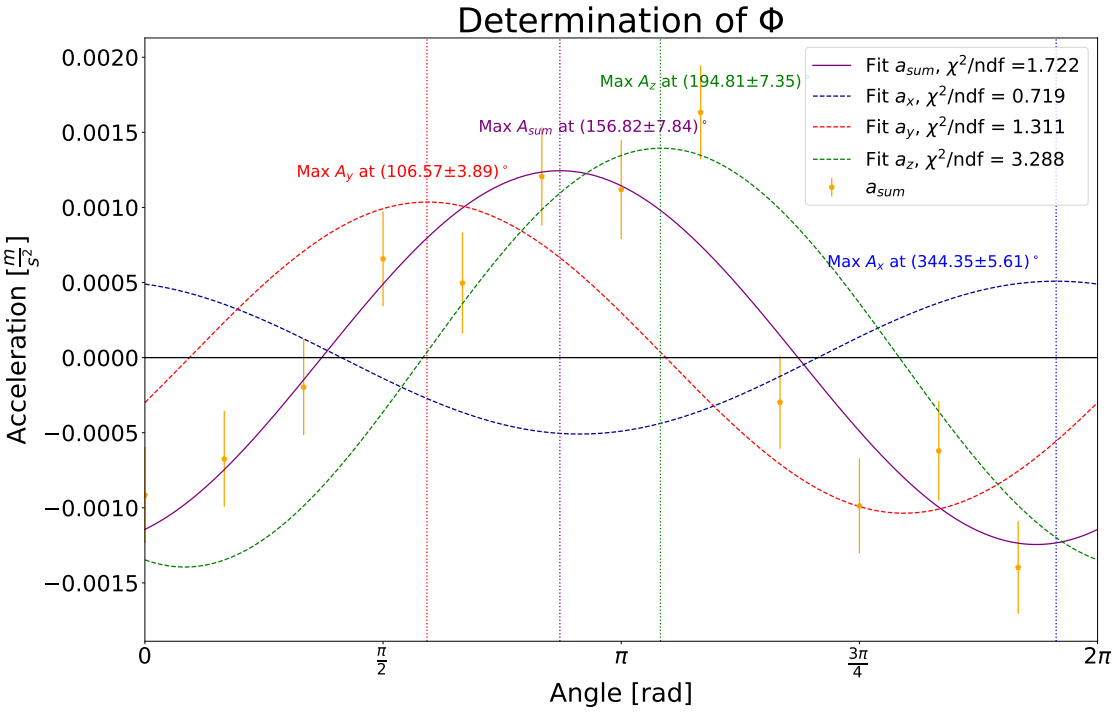

Figure 3.23: Four cosine curves, the three fitted curves for the acceleration data and the purple curve fitted to the sum of those three (orange) are shown. The x-coordinate of the maximum of the purple sine yields the azimuth angle of inclination for this measurement. The data points calculated for the summed curve can be seen in orange.

The fitting parameters for a_{i} can be found in Tab. 3.9.
Using the fitting parameters of the summed curve, the azimuth angle of the maximum can be deducted from the phase parameter $B = (2.737 \pm 0.137)$ rad $= (156.82 \pm 7.84)\,^\circ = \varphi$. The amplitude is given with $A = (0.0012 \pm 0.0002)\frac{\mathrm{m}}{\mathrm{s}^2}$.
Using this angle, it is difficult to set up the mount more precise, as the azimuth angle of inclination is given in an $\approx 8\,^\circ$ interval. It would be necessary to check if it is possible to align the mount with higher precision using this information of azimuth angle and how to increase the sensitivity of azimuth angle determination. Though, the calculations yield an approximation of azimuth angle of inclination.

3.4 Measuring angular accuracy outside of the lab

In this section, the mount is set up outside of the lab to validate the methods presented before on an uneven, not necessary solid ground. This is important, as the mount is expected to be set up in the field later on, where a solid ground can not be guaranteed. The measurement outside was executed on the *Flügelhügel* near the university, a picture of the setup can be found in appendix C. The mount was placed on an uneven ground with grass and soil. Two measurements are done. The plots for the inclination determination of the first measurement can be found in Fig. 3.24-3.26.

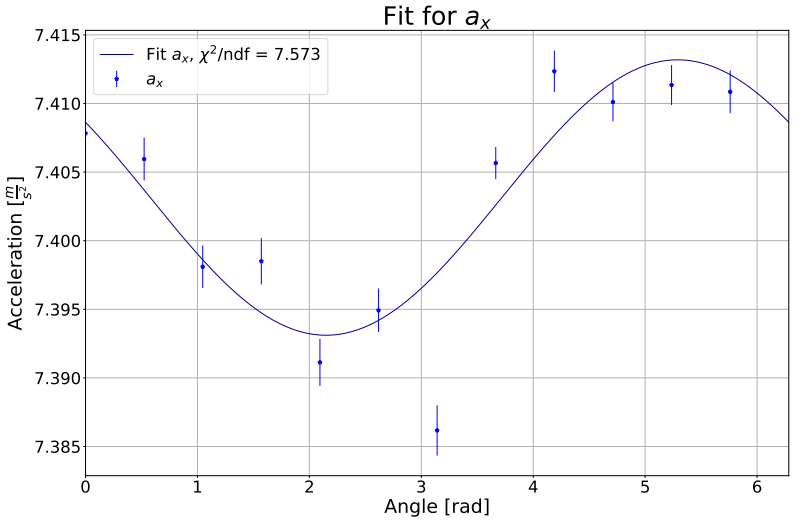

Figure 3.24: a_x component of the first measurement outside.

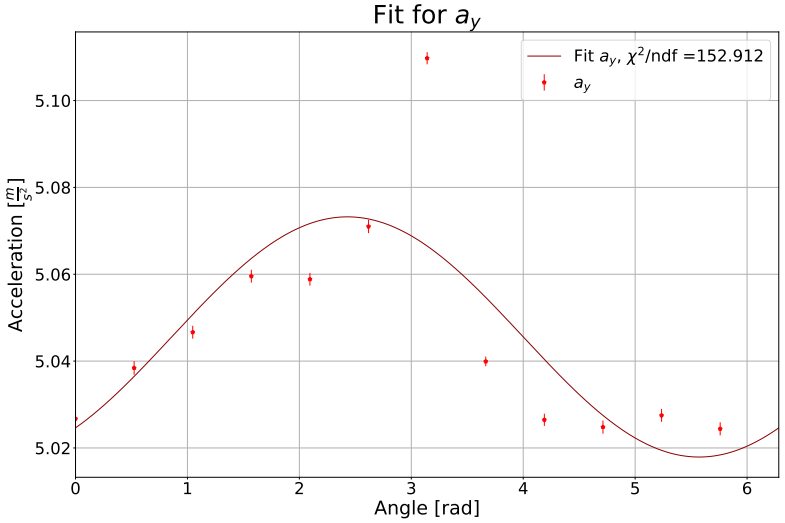

Figure 3.25: a_y component of the first measurement outside.

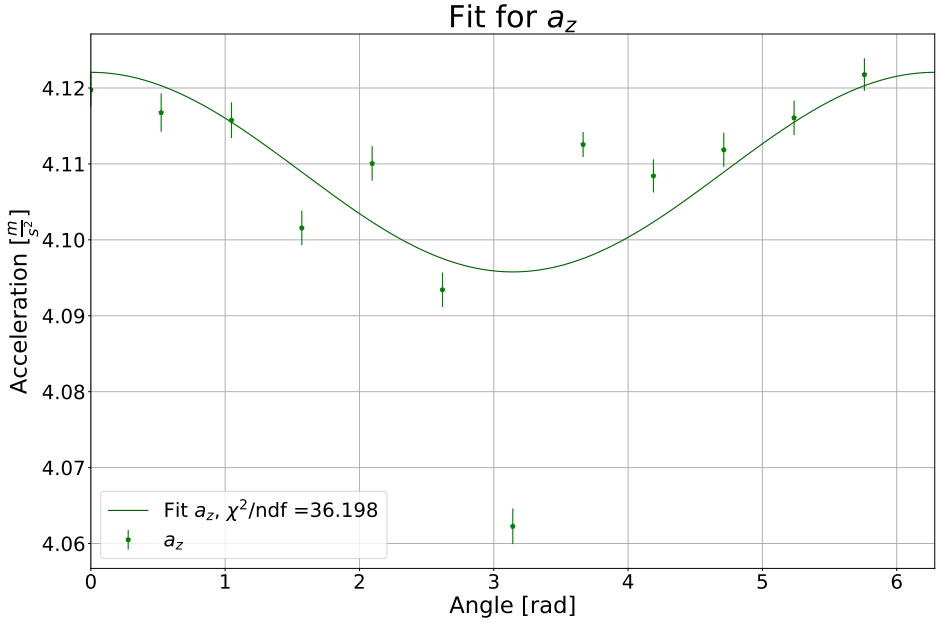

Figure 3.26: a_z component of the first measurement outside.

The fitting parameters can be found in Tab. 3.12.

Table 3.12: The table shows the Fitting parameters for the Fits seen in Fig. 3.24-3.26

	a_x	a_y	a_z
Amplitude A $[\frac{m}{s^2}]$	0.010 ± 0.002	0.027 ± 0.007	0.013 ± 0.005
Phase B [rad]	-0.99 ± 0.17	2.43 ± 0.26	0.00 ± 0.04
Offset C $[\frac{m}{s^2}]$	7.403 ± 0.001	5.046 ± 0.005	4.109 ± 0.004

In Fig. 3.25, the comparatively small uncertainties in relation to the amplitude of the oscillation of the data on each value are striking, as they lead to a value of $\chi^2/\text{ndf} = 152.9$. A fit with this high χ^2/ndf is not really significant. The uncertainty on both other components in relation to the amplitude of the oscillation is not that small. Also, the measurement at $\varphi = 180\,^\circ = 2\pi\,\text{rad}$ shows high deviants to the expected cosine course in all three components, which is not coherent with the circumstance of apparent higher precision of this measurement. The combination of small uncertainties on each value, resulting from a low standard deviation of the set of data from the mean, with the less sinusoid behaviour is not reasonable, as the course of the data should fit better to a sinusoid curve when the uncertainty is low. Vibrations or movement of the mount can be excluded as source of uncertainty, as the standard deviation on each value is not significantly big. A further investigation would be necessary to find the reason for both the low uncertainties and the deviation at $\varphi = 180\,^\circ$. Nonetheless, the angle of inclination

is calculated using the method described in Chap. 3.3.6. This yields an inclination of

$$\theta_{\text{Outside,1}} = (0.121 \pm 0.016)\,^\circ.$$

The azimuth angle can be calculated as described in Chap. 3.3.9. The fits for all components and the summed curve can be found in Fig. 3.27.

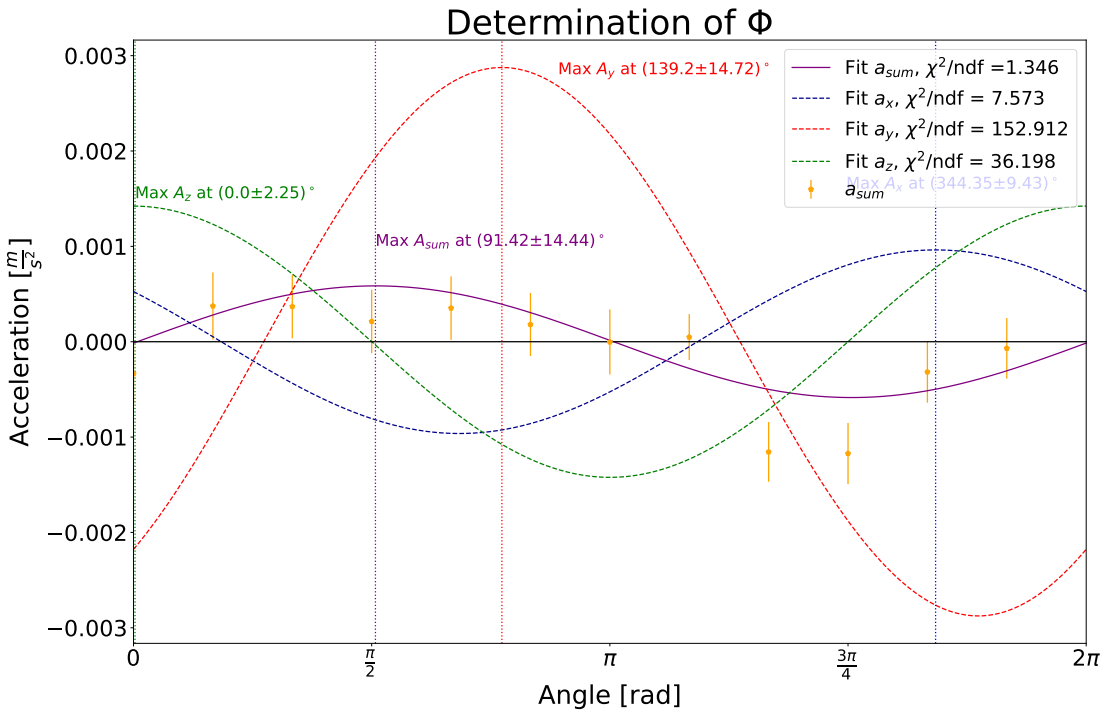

Figure 3.27: Four cosine curves, the three fitted curves for the acceleration data and the purple curve for the sum of those three.

The fitting parameters for a_{i} can be found in Tab. 3.12, the fitting parameters for the summed curve can be found in Tab. 3.13.

Table 3.13: The Fit parameters for the summed curve of the first measurement outside.

	a_{sum}
Amplitude A [$\frac{m}{s^2}$]	0.0006 ± 0.0002
Phase B [rad]	1.596 ± 0.252

Using this fit, the azimuth angle can be estimated to

$$\varphi_1 = (91.42 \pm 14.44)\,^\circ.$$

The uncertainty on this value is 14.44 °, which is significantly higher than the uncertainty determined in Chap. 3.3.9, which is possibly reasoned in the low quality fit of the a_y component. It is noticeable that the sum of all three components fits better to a sinusoidal curve than each of the components individually. Both the inclination angle and the azimuth angle of this measurement can not be used for further analysis, as the fit for the a_y component is not of sufficient accuracy.

In the following the second measurement outside of the university at a slightly different location is presented.

The plots for this measurement can be found in Fig. 3.28-3.30.

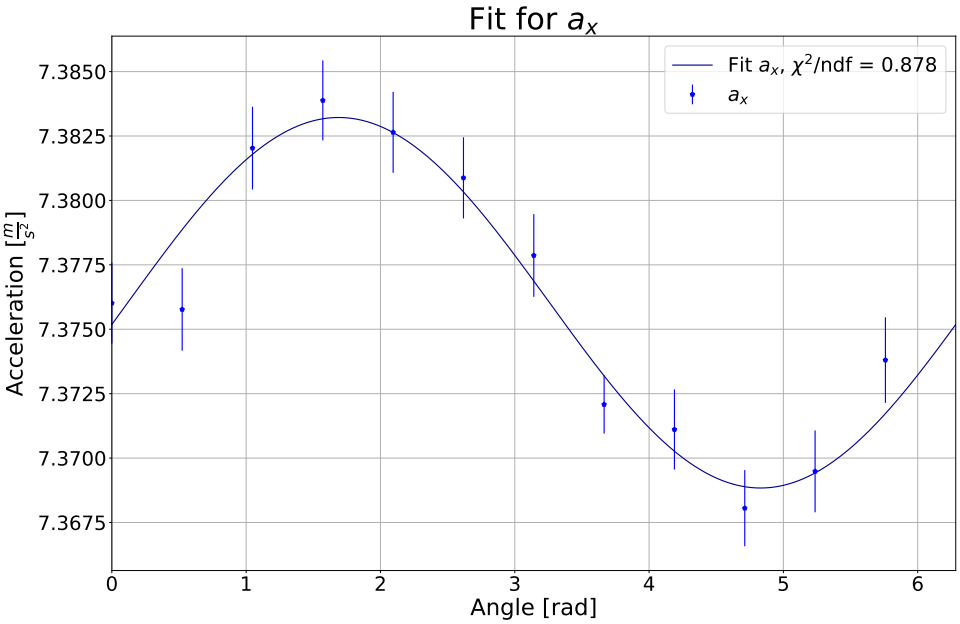

Figure 3.28: a_x component of the second measurement outside .

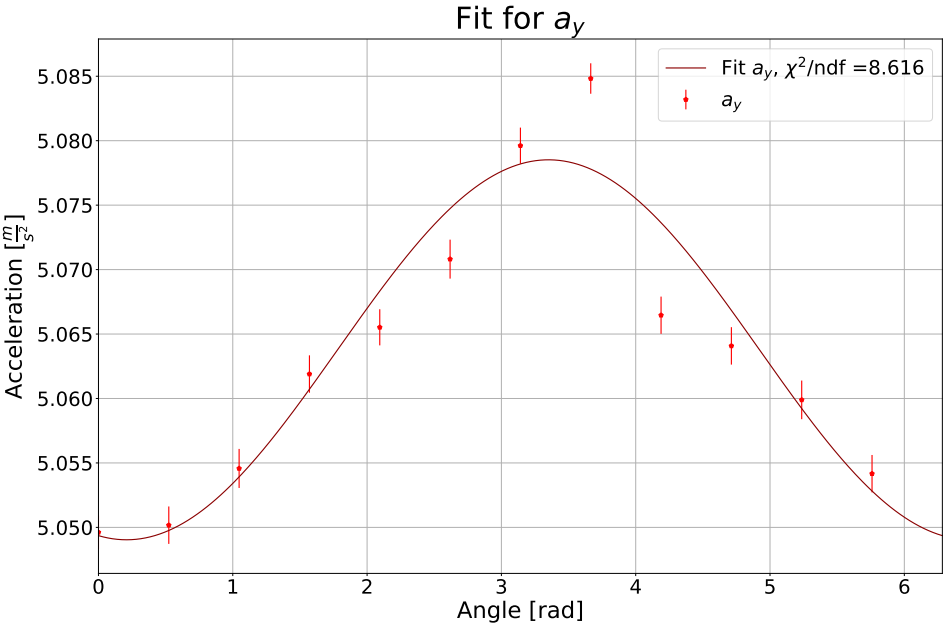

Figure 3.29: a_y component of the second measurement outside.

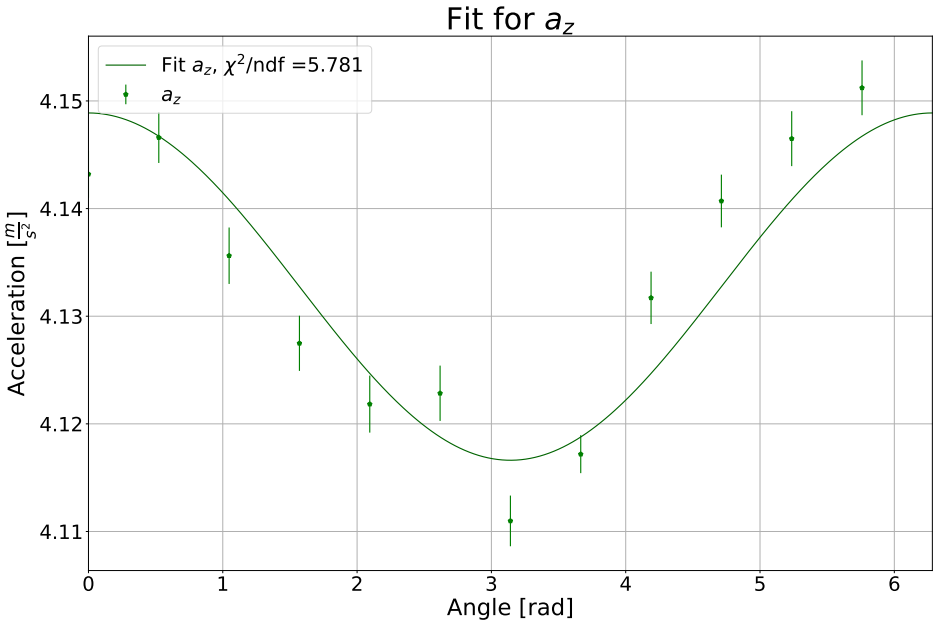

Figure 3.30: a_z component of the second measurement outside.

The fitting parameters can be found in Tab. 3.14.

Table 3.14: The Fit parameters for Fig. 3.28-3.30

	a_x	a_y	a_z
Amplitude A $[\frac{m}{s^2}]$	0.0072 ± 0.0006	0.015 ± 0.002	0.016 ± 0.002
Phase B [rad]	1.69 ± 0.08	3.35 ± 0.12	0.00 ± 0.21
Offset C $[\frac{m}{s^2}]$	7.376 ± 0.001	5.063 ± 0.001	4.133 ± 0.002

Figures 3.28-3.30 show that the quality of the fits of the second measurement is higher than those of the first, as the χ^2/ndf of all three fits is better than in the first measurement. The calculated cosine curve for every components fits better to the data points, which is another indication that the first measurement is containing errors. The angle of inclination can be determined to

$$\theta_{\text{Outside,2}} = (0.090 \pm 0.005)\,^\circ$$

The angle of inclination for this measurement is about $0.02\,^\circ$ bigger than the angle determined in the basement. Though, this measurement yields an inclination lower than the desired $< 1\,^\circ$ as described in Chap. 3.1.

The azimuth angle of the second measurement is determined in the following. At first, the summed curve is displayed in Fig. 3.31.

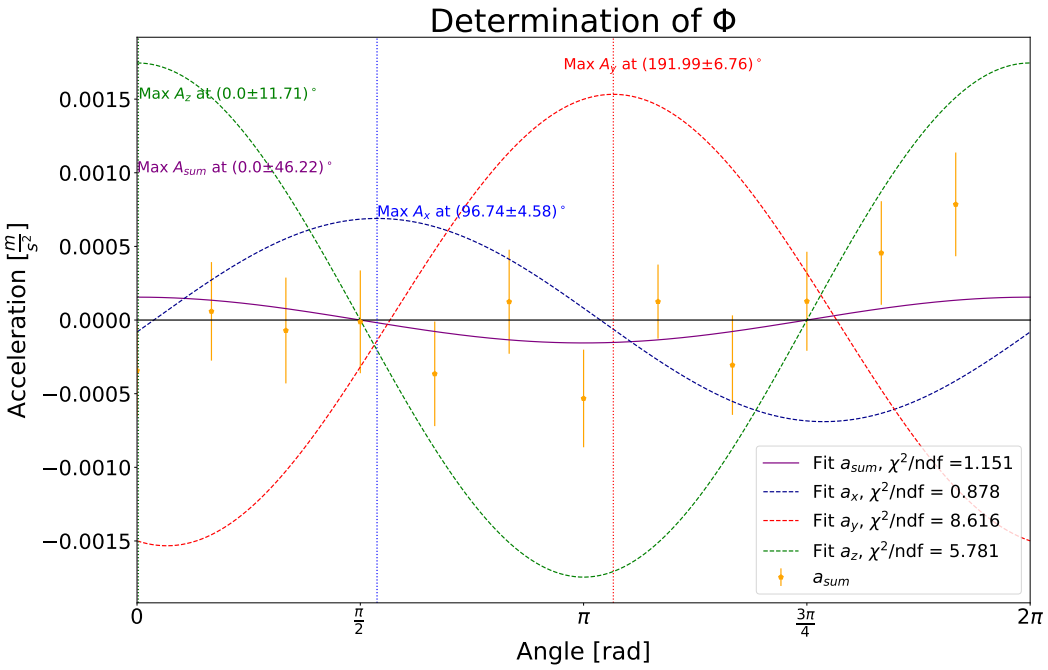

Figure 3.31: Four cosine curves, the three fitted curves for the acceleration data and the purple curve for the sum of those three.

The fitting parameters for a_{i} can be found in Tab. 3.14, the fitting parameters for the summed curve can be found in Tab. 3.15.

Table 3.15: The Fitting parameters for the summed curve of the second measurement outside.

	a_{sum}
Amplitude A $[\frac{m}{s^2}]$	0.0002 ± 0.0001
Phase B [rad]	0.00 ± 0.81

By looking at Fig. 3.31, one can see the oscillation of the summed data points is not clearly distinguishable, making it difficult to fit a cosine curve to the data points. The azimuth angle can be calculated using the phase parameter in Tab. 3.15 to

$$\varphi_2 = (0.00 \pm 46.22)\,^\circ.$$

This result is not really significant, as the uncertainty is very high. This is due to the sum of the data points leading to a small oscillation. A further elaboration on the sum of the data points could be expedient to resolve the sinusoidal oscillation in more detail. As both measurements outside of the university do not lead to a significant value for both inclination and azimuth angle at the same time, it is important to do more measurements outside of the laboratory to improve the quality of measurement to make use of the G-sensor when the mount is placed in the field. As seen in the second measurement, the inclination angle could be estimated resulting in a bubble level accuracy outside of the basement of $\theta_{\mathrm{Outside,2}} = (0.090 \pm 0.005)\,^\circ$.

4 Summary

In this thesis, several measurements using the telescope mount were executed. The necessary angular accuracy of the mount was determined to be $< 1°$. To test this accuracy, first a laser level was used to determine the accuracy of the bubble level. The angle of inclination when the mount was set up with the bubble level was determined to

$$\theta_{\text{Centered, laser level}} = (0.0594 \pm 0.0469)\,°.$$

This value is not satisfactory, as the uncertainty is of the same magnitude as the value of inclination. The high uncertainty could be justified in the insufficient accuracy of the laser level.
Another approach of angle measurement was done using an acceleration sensor attached to the telescope mount. Using the rotational invariance of acceleration when aligned with zenith, the inclination of the telescope mount aligned with the bubble level in the basement was determined to

$$\theta_{\text{Centered, sensor}} = (0.061 \pm 0.003)\,°.$$

This result is sufficient, as the angle is significantly lower than the necessary $< 1\,°$.
Furthermore, a comparison of the measurement at different locations was done. This comparison shows that the measurement in the basement is about 2 % more accurate than the measurement in the laboratory, which could be justified by vibrations of the building at higher floors. A comparison with a measurement on a hill outside was also done with the result of the measurement in the basement having a 2.4 % higher precision.
In the penultimate section, the azimuth angle of inclination is estimated. For the inclination measurement used before, the azimuth angle could be determined to be

$$\varphi = (156.82 \pm 7.84)\,°.$$

More tests are needed to ensure the uncertainty of $7.84\,°$ is low enough to use this angle for correcting the inclination using the G-sensor.
In the last chapter, the mount is set up outside of the building to verify the angular accuracy of the mount when set up on uneven, soft ground. Two measurements were done, resulting in the following inclinations:

$$\theta_{\text{Outside,1}} = (0.121 \pm 0.016)\,°$$

and

$$\theta_{\text{Outside,2}} = (0.090 \pm 0.005)\,^\circ$$

Both measurements are larger than the inclination measurement in the basement of the university but still in the range of the desired angular accuracy. It is important to note that the first measurement is somewhat containing errors, as the data points only fit to a cosine curve very vaguely. The second measurement confirms the accuracy of the bubble level to be higher than the desired accuracy. The azimuth angle of inclination for the first measurement yields an uncertainty of $14.44\,^\circ$. This value is however not significant, as the measurement is containing an error in some way. The second measurement did not allow a precise measurement of azimuth angle, as the summed data point oscillation is very low, making a fit very difficult. This results in value for the azimuth angle of $\varphi_2 = (0.00 \pm 46.22)\,^\circ$. A further approach on the accuracy outside of the building is needed to use the G-sensor for determining the azimuth angle of inclination reliably. For this, more measurements at various places and at higher inclinations could be suggestive. Nevertheless, with the setup of the G-sensor together with the software to perform an automated measurement of inclination of the telescope mount, a key tool for a successful roving laser campaign has been developed.

A Error propagation

To calculate the uncertainty of a value, which is calculated out of several other values with each having a certain uncertainty, the Gaussian error propagation is used. The formula for the uncertainty of the value to be calculated is:

$$\Delta f = \sqrt{\sum_{i=1}^{N} \left(\frac{\partial f}{\partial x_i} \right)^2 \cdot \Delta x_i^2}. \tag{A.1}$$

In this equation, Δf is the uncertainty on the value x, N is the amount of variables x_i contributing to the value f, where f is the function defining the value to be calculated. Δx_i is the uncertainty of each variable x_i.

A.1 Inclination Error Laser Level Method

To determine the Uncertainty of the Laser Level Measurements, the following equation, based on the general formula, is used:

$$\sigma_{\theta,\text{Laserlevel}} = \sqrt{\left(\frac{-d}{(b^2+d^2)} \cdot \sigma_\text{b} \right)^2 + \left(\frac{b}{(b^2+d^2)} \cdot \sigma_\text{d} \right)^2} \tag{A.2}$$

In this equation, b is the distance from Laser Level to the wall and d the measured distance from levelled line to unlevelled line. σ_b and σ_d are the respective uncertainties, where Δd is given by the accuracy k_{exp} of the laser determined in Chap. 3.2.1 times the distance b of the respective measurement.

A.2 Inclination Error G-Sensor Method

Primary, the uncertainty on the maximum and minimum value of the acceleration needs to be calculated. This can be done by Eq. A.3.

$$\sigma_{a_i,\ \text{max/min}} = \sqrt{(\sigma_{C,i}^2 + \sigma_{A,i}^2)} \tag{A.3}$$

In Eq. A.3, $\sigma_{C,i}$ is the uncertainty of the fitting parameter for the offset C and $\sigma_{A,i}$ the uncertainty of the fitting parameter for the Amplitude A, each for the respective sensor component $i \in \{X, Y, Z\}$. The uncertainty for each angle of the maximum and minimum acceleration to the respective g is calculated in Eq. A.4.

$$\sigma_\theta = \sqrt{\left(\frac{-1 \cdot \sigma_a}{g \cdot \sqrt{1 - \frac{a^2}{g^2}}} \right)^2 + \left(\frac{a \cdot \sigma_g}{g^2 \cdot \sqrt{1 - \frac{a^2}{g^2}}} \right)^2} \tag{A.4}$$

σ_a is the uncertainty on the acceleration value a, given by the fit. σ_g is the uncertainty on the value for g_i, as calculated in Chap. 3.3.4. To calculate the error propagation resulting through the difference of two angles, Eq. A.5 is used.

$$\sigma_{\theta,\text{ difference}} = \frac{1}{2} \cdot \sqrt{\sigma_{\theta_2}^2 + \sigma_{\theta_1}^2} \tag{A.5}$$

σ_{θ_i} is the uncertainty for each of the two θ's, as determined with Eq. A.4. The factor $\frac{1}{2}$ is due to the fact that the inclination angle is half of the angle between minimal and maximal acceleration. Finally, the uncertainty given by calculating the mean is determined using Eq. A.6.

$$\sigma_{\theta,\text{Ges}} = \frac{1}{3} \cdot \sqrt{\sigma_{\theta X}^2 + \sigma_{\theta Y}^2 + \sigma_{\theta Z}^2} \tag{A.6}$$

In this equation, $\sigma_{\theta X}$ is the uncertainty determined with Eq. A.5, and $\sigma_{\theta Y}$ and $\sigma_{\theta Z}$ respectively for the other two components.

B Fitting parameters

Table B.1 shows the fitting parameters for the Gaussian fits used in Chap. 3.3.8.

Table B.1: The fitting parameters for the Gaussian fits in Chap. 3.3.8

	Basement	Laboratory	Outside
σ $[\frac{m}{s^2}]$	0.029 ± 0.001	0.037 ± 0.002	0.033 ± 0.001
μ $[\frac{m}{s^2}]$	8.315 ± 0.002	8.308 ± 0.002	7.381 ± 0.002
A	4.2 ± 0.2	4.7 ± 0.2	4.4 ± 0.2
height	58 ± 3	51 ± 3	52 ± 3

C Pictures

In this section, a picture of the mount set up outside of the university can be found.

Figure C.1: The picture shows the mount set up outside of the university on grass.

References

[1] V. Hess, *über Beobachtungen der durchdringenden Strahlung bei sieben Freiballonfahrten.* Physik. Zeitschrift XIII, Pages 1084-1091 (1912)

[2] J. Matthews, *A Heitler model of extensive air showers.*
Retrieved from `http://particle.astro.ru.nl/ps/astropart1415-wk7a.pdf`
Last access: 04.09.2021
DOI: `10.1016/j.astropartphys.2004.09.003`

[3] P.A. Zyla et al. (Particle Data Group), Prog. Theor. Exp. Phys. 2020, 083C01, Page 514 (2020)
DOI: `https://doi.org/10.1093/ptep/ptaa104`

[4] A. Bucholtz, *Rayleigh-scattering calculations for the terrestrial atmosphere.*, Appl. Opt. 34, 2765-2773 (1995)
DOI: `https://doi.org/10.1364/AO.34.002765`

[5] R. Penndorf, *Tables of the refractive index for standard air and the Rayleigh scattering coefficient for the spectral region between 0.2 and 20.0 μ and their application to atmospheric optics.* Page 176 (1955)
DOI: `https://doi.org/10.1364/JOSA.47.000176`

[6] S. Chandrasekhar, *Radiative Transfer.* Page 49 (1960)

[7] The Pierre Auger Collaboration, *The Pierre Auger Observatory Upgrade - Preliminary Design Report.* (2015)
arXiv: 1604.03637

[8] C. Hernandez, *Studies of the atmospheric vertical aerosol optical depth and other applications to cosmic ray measurements.* (2017)
GAP2017_040

[9] The Pierre Auger Collaboration, *The Fluorescence Detector of the Pierre Auger Observatory* (2009)
arXiv: 0907.4282

[10] J. Matthews, *Optical Calibration of the Auger Fluorescence Telescopes.* (2002)
GAP2002_029

[11] M. Roberts et al., *May 2005 laser absolute calibration of the Coihueco and Los Leones fluorescence detectors.* (2005)
GAP2005_089

[12] M. Roberts et al., *Absolute calibration of the Auger fluorescence detectors using atmospheric laser beams.* (2003)
arXiv: astro-ph/0507347

[13] Pierre Auger Collaboration (2021), *Auger Open Data release 1-2021*
DOI:10.5281/zenodo.4487613
Retrieved from: https://labdpr.cab.cnea.gov.ar/opendata/data.php
Last access: 04.09.2021

[14] Private communication *A. Nasr-Esfahani*

[15] W. Torge, J. Müller, *Geodesy.* Page 47 (2012)

[16] iOptron Corporation, *iOptron AZ Mount Pro Altazimuth Mount Instrucion Manual.*

[17] BHPhotovideo, *Sales page.*
Retrieved from https://www.bhphotovideo.com/c/product/1529941-REG/ioptron_8903_az_mount_pro_with.html
Last access: 14.09.2021

[18] C. Woodford, *Accelerometers.* (2009/2020)
Retrieved from https://www.explainthatstuff.com/accelerometers.html
Last access: 26.7.2021

[19] C. Fisher, *AN-1057: Using an Accelerometer for Inclination Sensing.*
Retrieved from https://www.analog.com/en/app-notes/an-1057.html
Last access: 26.7.2021

[20] Bosch *GLL 2-10 Professional Original Instructions.*
Retrieved from https://www.bosch-professional.com/binary/ocsmedia/optimized/full/o335479v21_160992A4HJ_202006.pdf
Last access: 04.09.2021

[21] digikey *MPU 6050 Acceleration sensor*
https://www.digikey.de/product-detail/de/3886/1528-3886-ND/10709725
Last access: 16.09.2021

[22] digikey *ESP32-DEVKITC-32E*
https://www.digikey.de/product-detail/de/ESP32-DEVKITC-32E/1965-ESP32-DEVKITC-32E-ND/12091810
Last access: 16.09.2021

[23] *ESP32 with MPU-6050 Accelerometer, Gyroscope and Temperature Sensor.*
Retrieved from
https://randomnerdtutorials.com/esp32-mpu-6050-accelerometer-gyroscope-arduino/
Last access: 05.09.2021

[24] Arduino open-source electronics platform
`https://www.arduino.cc/`
Last access: 02.09.2021

[25] FreeCAD 3D parametric modeling system
`https://www.freecadweb.org/`
Last access: 02.09.2021

[26] LMFit *Non-Linear Least-Squares Minimization and Curve-Fitting for Python.*
`https://lmfit.github.io/lmfit-py/`
Last access: 02.09.2021

[27] *Hinweise zur Beurteilung von Messungen, Messergebnissen und Messunsicherheiten*
Retrieved from: `https://www.ph.tum.de/academics/org/labs/ap/org/ABW.pdf`
Last access: 28th August 2021

[28] Laser Simulation done by Alina Nasr-Esfahani

[29] Literature value for g in Wuppertal.
`https://www.ptb.de/cms/ptb/fachabteilungen/abt1/fb-11/fb-11-sis/g-extractor.html`
Last access: 09.09.2021

[30] The developed scripts can be found at: `https://git.uni-wuppertal.de/buw-auger/rovinglaser/-/tree/master/scrpt` or by contacting Alina Nasr-Esfahani

Acknowledgements

At first, I would like to thank *Prof. Dr. Karl-Heinz Kampert* for helping me finding the topic for this work and giving me the opportunity to write this thesis. Furthermore, I want to thank *Prof. Dr. Ralf Koppmann* for volunteering as the co-corrector of this thesis without hesitation.

The relentless support from *Alina Nasr-Esfahani* made it possible for me to work on various parts of this thesis, giving me the possibility to learn a lot of new things, whether it was soldering, programming, data analysis, literature research or scientific writing.

Both *Dr. Julian Rautenberg* and *Dr. Eric Mayotte* spent a lot of their time thinking about my problems, explaining things and helping me patiently when I needed assistance, which I am also very grateful for.

I also have to thank *Dennis Pfeifer* for helping me patiently with the CAD designs and the work on the 3D printer. This saved me a lot of time working on the perfect fit for the Case.

Also I want to thank *Urs* and *Jannis* for always giving me some good advice when I needed it and always made the office-atmosphere very relaxed.

Without the support of my friends, this thesis would have been a lot more difficult, as they helped me with both my thesis on the one hand and the lecture I had parallel to the thesis on the other hand. My gratitude to *Lukas, Niklas, Emil, Max, Gianluca* and especially *Philip* is immeasurable.

At last I want to show my deepest gratitude to *Marie* for helping me carrying all my burdens throughout most of my time at the university, especially the past three months, and to my father *Stefan* for always lending me his time when I needed it and also for reminding me that some leisure time is always great.

Name, Vorname: Kleu, Patrick

Erklärung

gem. §15 Abs. 6 der Prüfungsordnung vom 25.11.2019

Hiermit erkläre ich, dass ich die Bachelor-Thesis selbstständig verfasst und keine anderen als die angegebenen Quellen und Hilfsmittel benutzt sowie Zitate kenntlich gemacht habe.

....

Datum Unterschrift

Erklärung

Hiermit erkläre ich mich damit einverstanden, dass meine Abschlussarbeit (Bachelor-Thesis) wissenschaftlich interessierten Personen oder Institutionen und im Rahmen von externen Qualitätssicherungsmaßnahmen des Studienganges zur Einsichtnahme zur Verfügung gestellt werden kann.
Korrektur- oder Bewertungshinweise in meiner Arbeit dürfen nicht zitiert werden.

....

Datum Unterschrift